

PAPER • OPEN ACCESS

# Recovery of release cloud from laser shock-loaded graphite and hydrocarbon targets: in search of diamonds

To cite this article: A K Schuster *et al* 2023 *J. Phys. D: Appl. Phys.* **56** 025301

View the [article online](#) for updates and enhancements.

You may also like

- [The Effect of Shock-wave Duration on Star Formation and the Initial Condition of Massive Cluster Formation](#)  
Daisei Abe, Tsuyoshi Inoue, Rei Enokiya et al.
- [V E Fortov and dynamic methods in nonideal plasma physics. Chernogolovka](#)  
V B Mintsev and V K Gryaznov
- [MHD Simulations of Dense Core Collision](#)  
Shinichi W. Kinoshita and Fumitaka Nakamura

# Recovery of release cloud from laser shock-loaded graphite and hydrocarbon targets: in search of diamonds

A K Schuster<sup>1,2,24,\*</sup>, K Voigt<sup>1,2</sup>, B Klemmed<sup>3</sup>, N J Hartley<sup>1,4</sup>, J Lütgert<sup>1,2,5</sup>, M Zhang<sup>1,6</sup>, C Bähz<sup>1</sup>, A Benad<sup>3</sup>, C Brabetz<sup>7</sup>, T Cowan<sup>1,2</sup>, T Döppner<sup>8</sup>, D J Erb<sup>9</sup>, A Eychmüller<sup>3</sup>, S Facsko<sup>9</sup>, R W Falcone<sup>10,11</sup>, L B Fletcher<sup>4</sup>, S Frydrych<sup>8,12</sup>, G C Ganzenmüller<sup>13</sup>, D O Gericke<sup>14</sup>, S H Glenzer<sup>4</sup>, J Grenzer<sup>9</sup>, U Helbig<sup>1</sup>, S Hiermaier<sup>13</sup>, R Hübner<sup>9</sup>, A Laso Garcia<sup>1</sup>, H J Lee<sup>4</sup>, M J MacDonald<sup>4,15</sup>, E E McBride<sup>4,16</sup>, P Neumayer<sup>7</sup>, A Pak<sup>8</sup>, A Pelka<sup>1,16</sup>, I Principe<sup>1</sup>, A Prosvetov<sup>17</sup>, A Rack<sup>18</sup>, A Ravasio<sup>19</sup>, R Redmer<sup>5</sup>, D Reemts<sup>7</sup>, M Rödel<sup>1,2</sup>, M Schoelmerich<sup>8,16</sup>, D Schumacher<sup>7</sup>, M Tomut<sup>17</sup>, S J Turner<sup>20,21,22,23</sup>, A M Saunders<sup>10</sup>, P Sun<sup>4</sup>, J Vorberger<sup>1</sup>, A Zettl<sup>21,22,23</sup> and D Kraus<sup>1,5,\*</sup>

<sup>1</sup> Institute of Radiation Physics, Helmholtz-Zentrum Dresden-Rossendorf, 01328 Dresden, Germany

<sup>2</sup> Institute of Solid State and Materials Physics, TU Dresden, Haeckelstraße 3, 01069 Dresden, Germany

<sup>3</sup> Institute of Physical Chemistry, TU Dresden, Haeckelstraße 3, 01069 Dresden, Germany

<sup>4</sup> SLAC National Accelerator Laboratory, Menlo Park, CA 94309, United States of America

<sup>5</sup> Institute of Physics, Universität Rostock, Albert-Einstein-Str. 23, 18059 Rostock, Germany

<sup>6</sup> Department of Physics, University of Science and Technology of China, Hefei 230026, People's Republic of China

<sup>7</sup> Department of Plasma Physics, GSI Helmholtzzentrum für Schwerionenforschung GmbH, Planckstraße 1, 64291 Darmstadt, Germany

<sup>8</sup> Lawrence Livermore National Laboratory, Livermore, CA 94550, United States of America

<sup>9</sup> Institute of Ion Beam Physics and Materials Research, Helmholtz-Zentrum Dresden-Rossendorf, 01328 Dresden, Germany

<sup>10</sup> Department of Physics, University of California, Berkeley, CA 94720, United States of America

<sup>11</sup> Lawrence Berkeley National Laboratory, Berkeley, CA 94720, United States of America

<sup>12</sup> Institute of Nuclear Physics, TU Darmstadt, Schlossgartenstraße 9, 64289 Darmstadt, Germany

<sup>13</sup> Department of Sustainable Systems Engineering (INATECH), Albert-Ludwigs-Universität, D-79110 Freiburg, Germany

<sup>14</sup> Centre for Fusion, Space and Astrophysics, Department of Physics, University of Warwick, Coventry CV4 7AL, United Kingdom

<sup>15</sup> University of Michigan, Ann Arbor, MI 48109, United States of America

<sup>16</sup> European XFEL GmbH, Holzkoppel 4, 22869 Schenefeld, Germany

<sup>17</sup> Department of Materials Research, GSI Helmholtzzentrum für Schwerionenforschung GmbH, Planckstraße 1, 64291 Darmstadt, Germany

<sup>18</sup> Structure of Materials Group, ESRF—The European Synchrotron, 38000 Grenoble, France

<sup>19</sup> Laboratory for the Use of Intense Lasers (LULI), CNRS, CEA, Sorbonne Université, école Polytechnique, Institut Polytechnique de Paris, Palaiseau, France

<sup>20</sup> Department of Chemistry, University of California, Berkeley, CA, United States of America

<sup>21</sup> Department of Physics, University of California, Berkeley, CA, United States of America

<sup>22</sup> Materials Sciences Division, Lawrence Berkeley National Laboratory, Berkeley, CA, United States of America

<sup>23</sup> Kavli Energy NanoScience Institute, Berkeley, CA, United States of America

<sup>24</sup> Present address: Marvel Fusion, Theresienhöhe 12, 80339 München, Germany

\* Authors to whom any correspondence should be addressed.



Original Content from this work may be used under the terms of the [Creative Commons Attribution 4.0 licence](https://creativecommons.org/licenses/by/4.0/). Any further distribution of this work must maintain attribution to the author(s) and the title of the work, journal citation and DOI.

E-mail: [a.k.schuster@gmx.de](mailto:a.k.schuster@gmx.de) and [dominik.kraus@uni-rostock.de](mailto:dominik.kraus@uni-rostock.de)

Received 2 April 2022, revised 22 July 2022

Accepted for publication 13 October 2022

Published 9 December 2022



## Abstract

This work presents first insights into the dynamics of free-surface release clouds from dynamically compressed polystyrene and pyrolytic graphite at pressures up to 200 GPa, where they transform into diamond or lonsdaleite, respectively. These ejecta clouds are released into either vacuum or various types of catcher systems, and are monitored with high-speed recordings (frame rates up to 10 MHz). Molecular dynamics simulations are used to give insights to the rate of diamond preservation throughout the free expansion and the catcher impact process, highlighting the challenges of diamond retrieval. Raman spectroscopy data show graphitic signatures on a catcher plate confirming that the shock-compressed PS is transformed. First electron microscopy analyses of solid catcher plates yield an outstanding number of different spherical-like objects in the size range between ten(s) up to hundreds of nanometres, which are one type of two potential diamond candidates identified. The origin of some objects can unambiguously be assigned, while the history of others remains speculative.

Supplementary material for this article is available [online](#)

Keywords: recovery, nanodiamonds, laser-induced shock compression, high energy density

(Some figures may appear in colour only in the online journal)

## 1. Introduction

Material properties are only poorly understood and theoretically very difficult to describe in the transition regime between solid-state matter and a plasma [1–4], the so-called warm dense matter regime [5]. Here, the thermal energy of electrons is similar to those of chemical bond energies and above giving rise to extreme chemistry [6]. The rising number of high-energy laser facilities [7, 8] enables continuously improving access to these highly interesting states of matter in as yet uncharted parts of the phase diagrams of materials. One promising way to improve our understanding of materials under such extreme conditions as they are found in planetary and stellar environments is the performance of dynamic shock compression experiments investigating the processes by means of *in situ* and recovery methods.

Dynamic shock compression experiments can be realised using various techniques. Our experimental approach is based on a high-energy laser creating an upstreaming plasma on the front surface of a solid-state sample [9, 10]. This upstreaming plasma drives a shock wave through the remaining target obeying the conservation law for momentum. The shock wave compresses the target to extreme pressure and temperature conditions [11] relevant to stellar or planetary objects in our Universe (see figure 1(a)) [12–17]. In such an environment, the target species enter new regimes in which processes of extreme chemistry or phase separations can be triggered leading to a transformation of the initial sample. Eventually, the shock wave is reaching the sample rear-side where the material is expelled in an ejecta cloud. Only lately, x-ray free electron lasers emerged which deliver highly intense and ultra-short

(fs) x-ray pulses to probe such transient (ns) states *in situ* [18]. Thereby, the formation of numerous potentially metastable structures was demonstrated [12, 13, 19–23], whose recovery is highly desirable for an improved understanding of their formation process and possible applications of these materials. The main challenges are the small amount of material ( $<1\text{ mm}^3$ ) that is shock-compressed, the nano- to micrometre scale of the formed metastable objects, the open question of their preservation during the free expansion from their extreme states, and their high ejection velocities of up to tens of  $\text{km s}^{-1}$ .

The work presented here focuses on a first step towards the recovery of lonsdaleite, often referred to as hexagonal diamond, and cubic diamond formed in laser shock-loaded pyrolytic graphite (PG) and polystyrene (PS) samples, respectively [12, 13, 19]. Lonsdaleite formation in our experiments has so far only been achieved by dynamically compressing PG. The diamond particles originating from PS and PG samples are ejected after shock breakout in the course of a free-surface release as part of an ejecta cloud travelling at estimated maximum velocities up to  $\sim 20\text{ km s}^{-1}$ . High-speed recordings with frame rates of up to 10 MHz grant first insights into the dynamics of the evolving ejecta cloud and its impact into a variety of specially designed catcher systems. Their success at capturing intact diamond particles was evaluated using various post analysis techniques such as Raman spectroscopy, x-ray diffraction, tomography, as well as scanning and transmission electron microscopy. To date, two types of diamond candidates could be identified.

Generally, recovery of materials formed under transient extreme conditions is a concept that has been well established in light gas gun, flyer plate, and diamond anvil cell

experiments, as well as in space missions such as NASA's Stardust [24–29]. However, recovery of materials created during laser-driven shock compression experiments [22, 23, 30, 31] is still an emerging technique and is particularly underdeveloped in the high-pressure regime ( $>100$  GPa) relevant to this work [32, 33]. We want to close this gap and investigate various recovery concepts for nanometre-sized hexagonal and cubic diamond particles generated in laser shock-loaded graphite and hydrocarbon samples at pressures  $>100$  GPa.

## 2. Experiments

The recovery samples were collected during a series of experiments at the matter in extreme conditions end station of the Linac Coherent Light Source (LCLS) of the SLAC National Accelerator Laboratory [34, 35], at the ID 19 beamline of the European Synchrotron Radiation Facility (ESRF) [36, 37], and the Z6 endstation at the GSI Helmholtzzentrum für Schwerionenforschung GmbH [38]. A schematic of a representative set-up for all recovery experiments is illustrated in figure 1.

First, it was confirmed that the pressure and temperature conditions for cubic diamond (PG  $>50$  GPa and for PS  $\sim 150$  GPa,  $\sim 5000$  K) and lonsdaleite formation (PG  $>170$  GPa) were achieved. For that goal, velocity interferometer system for any reflector (VISAR) measurements [39] (see figure 1(a)) and 1D simulations with HELIOS [40] were performed. A flat top pulse for PG and a step pulse profile of the drive laser for PS targets were used to reach the predicted conditions for diamond formation [12, 13, 19] (see figure 20). The majority of PG targets in our experiments had a thickness of  $100\ \mu\text{m}$  and were coated with a  $100\ \text{nm}$  aluminium layer on the back surface for VISAR measurements. For recovery shots, non-coated targets were used to minimise contamination. The  $125\ \mu\text{m}$  thick PS targets were generally coated with  $100\ \text{nm}$  aluminium on the front surface to prevent target pre-heating by low-intensity pre-pulses from the drive laser. For some VISAR measurements, the PS target rear surface had a  $100\ \text{nm}$  aluminium coating to measure the shock breakout time.

After the shock breakout at the target rear surface, a cloud containing the diamond or lonsdaleite particles is ejected (see figure 1(b)). We deploy either a solid or aerogel catcher (see figures 1(c) and (d)) to retrieve these ejecta. The key components of a solid catcher, as shown in sub-image (c), are a catcher tube and a plate closing the volume behind the target. These plates are made from different materials such as high-purity metal ( $>99.9\%$  Al, Ti, Cu, or Ag) or pure quartz. The second type referred to as aerogel catcher uses the same design, with the addition of an inorganic aerogel inside the catcher tube (BN [41–43],  $\text{SiO}_2$ ,  $\text{ZrO}_2$ ,  $\text{Al}_2\text{O}_3$  annealed at various temperatures or doped with different percentages of zirconium [44]). The various aerogel types have different mechanical properties and are thus expected to show differences in their recovery performance [45]. Moreover, the high-speed impact of diamond particles into BN aerogel may enhance the diamonds' properties with electrical conductivity and fluorescence due to potential boron and nitrogen doping, respectively [46], which

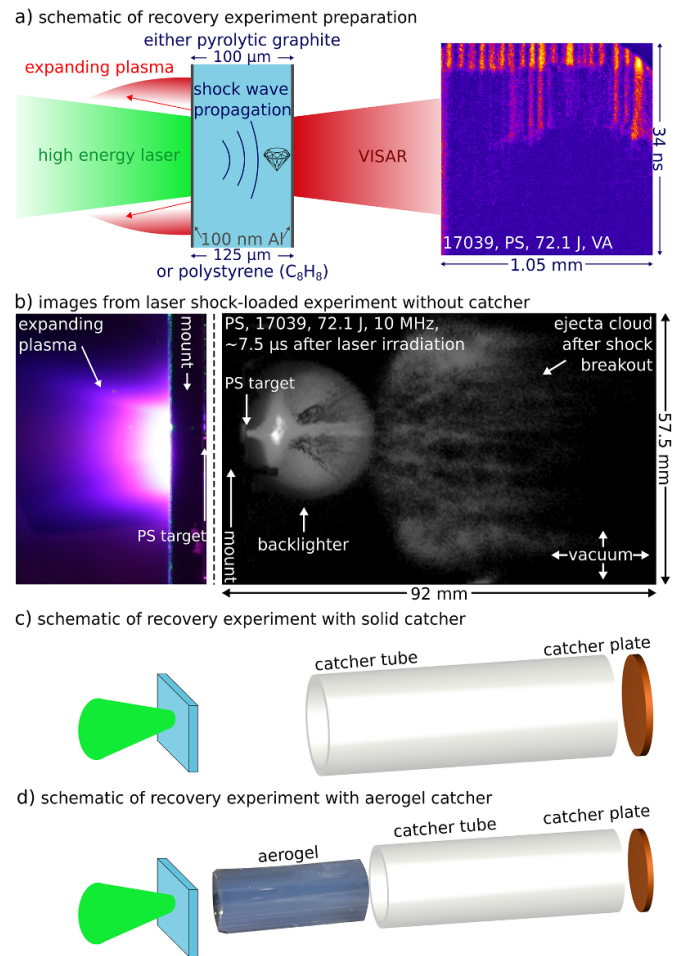


**Figure 1.** VISAR measurements were performed to confirm reaching the desired pressures in preparation for the recovery experiment (a). Reproduced from [33]. CC BY 4.0. Optical images of the upstreaming plasma on the target front surface and a free-surface release cloud expected to contain the diamond particles are shown in sub-image (b). The exploded-view schematic of the key components of a solid catcher being centred behind the target for recovery of the ejected material is shown in (c). Likewise, the second major recovery type, the aerogel catcher (d), uses the same key components as the solid catcher but additionally holds an aerogel inside its tube.

is very interesting in terms of applications. Another type of catcher cylinder was filled with organic gel (Crystal-Kerzen-Gel from CREARTEC trend design GmbH) since it is known for its soft recovery properties (see figures 15(a)–(c)) [30, 31]. It was tested but not prioritised due to the potentially ambiguous carbon origin of the formed diamond particles. One set of recovery samples was specifically handled in a clean-room class 1000.

## 3. Results and discussion

### 3.1. Molecular dynamics simulation: free expansion scenarios

Molecular dynamics (MD) simulations were performed using the LAMMPS MD Simulator [47] to obtain approximations

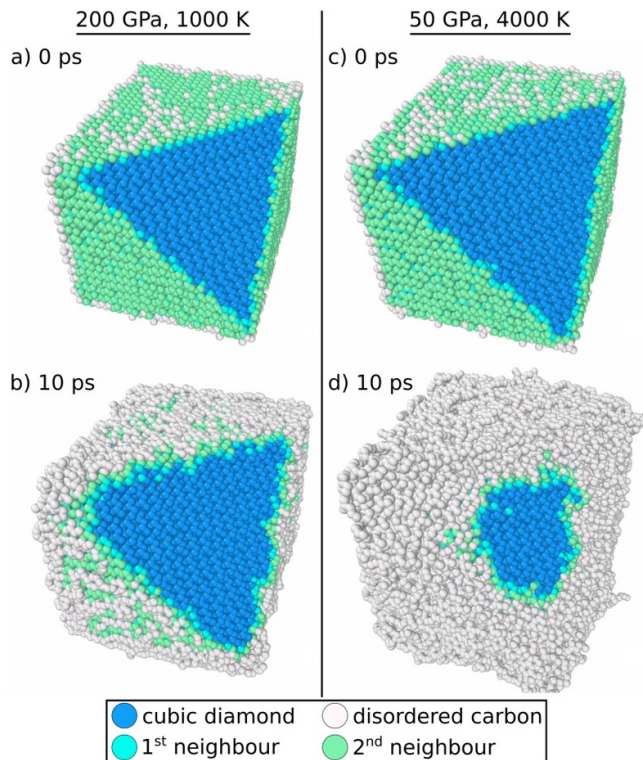


**Figure 2.** MD simulations modelling the free expansion of a diamond cuboid with dimensions of  $\sim(6 \times 5 \times 4) \text{ nm}^3$  consisting of 43 008 atoms from 200 GPa and 1000 K (a), (b) as well as 50 GPa and 4000 K (c), (d) for a time period of 10 ps. Reproduced from [33]. CC BY 4.0. Carbon atoms in the cubic diamond lattice and disordered ones are represented in blue and light-grey, respectively. Turquoise and green carbon atoms represent the edge of a diamond structure, where they have less neighbours than a central carbon atom in the diamond lattice.

for the preservation limit of diamond (1) relaxing in a free expansion from 200 GPa and 1000 K as well as 50 GPa and 4000 K (see figure 2), and (2) in various impact scenarios into aluminium (see figure 7). Diamond and aluminium were modelled using the adaptive intermolecular reactive empirical bond order potential (AIREBO-M) [48] and the potential based on the embedded-atom method [49]. The potentials were validated by agreeing with the established equation of state for diamond and aluminium by reproducing the pressures and temperatures behind the shock front. Initially, all diamond crystallites were equilibrated for 100 ps in an isobaric, isothermal ensemble of constant number of particles (NPT) with periodic boundary conditions. The simulation parameters were chosen to get the best results from the resources that were available at the time of preparing this manuscript. More advanced MD simulations are work in progress.

Subsequently, free expansion (see figure 2) or, as shown later, impact (see figure 7) was modelled in an adiabatic ensemble of constant NPT. The simulation time was 10 ps. It is evident that the structure is more sensitive to higher temperature compared to higher pressure in the free expansion process. It is encouraging that even in the high-temperature scenario (50 GPa, 4000 K), being close to the diamond melting line [50], a diamond core is still present after 10 ps. In reality,

we expect these results to underestimate the preservation limit since the dissipative process of radiation cooling is neglected in this picture. Moreover, the simulated nanodiamond particle is on the lower part of the anticipated size range and therefore more sensitive to pressure and temperature changes and the characteristic signature of diamond was still observable multiple nanoseconds after shock breakout at scattering angles consistent with ambient density in *in situ* x-ray diffraction data of laser shock-loaded PS in [12]. Therefore, it is assumed that the diamonds generated in laser-driven shock-compressed graphite and PS stay preserved during their free expansion and impact as high-speed projectiles into the catcher systems. Hence, a tailoring of the release path has not yet been considered necessary [23]. In general, higher ejection velocities are obtained from samples irradiated with a step pulse compared to a flat top laser pulse, but in our experiments, much higher pulse energies were used for the graphite samples to reach the regime where lonsdaleite has been observed by *in situ* XRD in a previous experiment [19].

### 3.2. Impact dynamics

Material not fully converted to diamond, for example defective graphite remnants (PG) or hydrocarbons of various stoichiometry (PS), are expected to impact into the catcher systems alongside the diamonds [12, 13]. These materials are assumed to impact at hypervelocities; i.e. velocities high enough that material strength becomes negligible and its behaviour can be described as that of a fluid [51, 52].

Diamond, on the other hand, is expected to remain solid as the conditions are below the melt line on the shock Hugoniot ( $>600 \text{ GPa}$  and  $\sim 9000 \text{ K}$ ) [50]. However, the boundaries in the carbon phase diagram are known to depend on the diamond particle size; the smaller the particle size the more do the boundaries shift towards higher temperature sensitivity for the diamond phase [53–56]. The diamond particle sizes in our laser shock-loaded PS can be estimated between 4–100 nm at the moment the *in situ* XRD data were recorded [14]. Ongoing efforts using small-angle x-ray scattering aim to get a more accurate knowledge about the particle size distribution [13, 57], and experiments with significantly longer delays than 7 ns between pump and probe laser are planned. It is possible that the diamond particles observed during *in situ* XRD keep growing in the warm dense plasma cloud to substantially larger sizes. The diamond size distribution originating from a shock-compressed graphite target is expected to be notably shifted to larger sizes in the micrometre range compared to the one of PS in the nanometre to tens or even hundreds of nanometres range, which may be explained by their different formation processes. While graphite transforms in a solid-solid transition to cubic or hexagonal diamond [58] when irradiated with a suitable flat top laser pulse, PS undergoes a disordered formation process in the warm dense matter regime involving chemical reactions when irradiated with an appropriate step laser pulse. In the latter case, the diamond formation process is so far only poorly understood. A possible explanation is that the first shock wave leads to the dissociation of PS polymers and the second shock wave possibly triggers

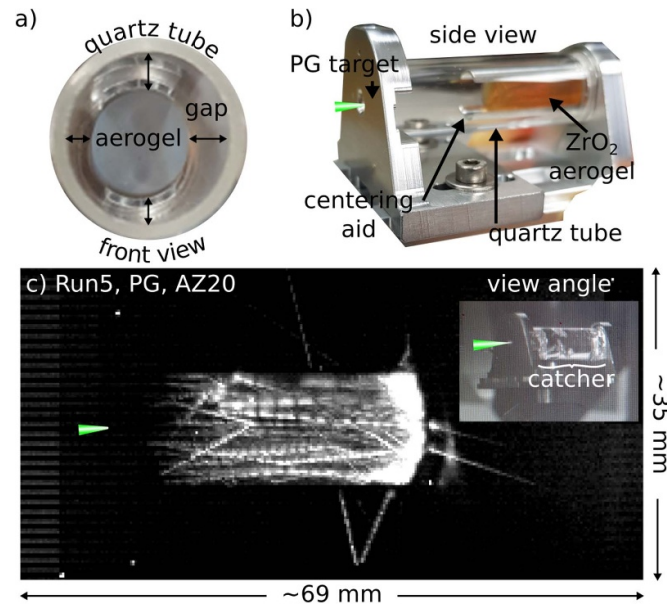


**Figure 3.** Laser-driven shock compression experiment with a 5-J pump laser reaching up to 50 GPa in pyrolytic graphite targets at the ID19 beamline at ESRF. Reproduced from [33]. [CC BY 4.0](#). (a) A front view into the catcher shows the aerogel being centred in a quartz cylinder. (b) Design of target-catcher complex. (c) The trajectories of light-emitting particles ejected after shock breakout into the catcher and impacting into an  $\text{Al}_2\text{O}_3$  aerogel doped with 20% zirconium (AZ20). The maximum projection of all frames was generated from a high-speed video recorded with a Photron FASTCAM SA1.1 model 675K-M3 at a frame rate of 125 kHz. The Fluorescence Image Evaluation Software for Tracking and Analysis (FIESTA) was used to obtain the maximum projection [73].

the insulator-metal transition of hydrogen [59, 60]. Diamond nucleation seeds may form with carbon not being soluble in metallic hydrogen [14, 33]. Efforts towards a better understanding of this formation process are ongoing among others in the framework of post analysis of recovered material. A potential size difference between diamonds produced from PG and PS targets may have observable effects on their preservation due to differing boundaries in their phase diagrams.

In general, the main difference between the two main impact types are impacts into either solid-density or low-density catchers with catcher density to projectile density ratios of  $\sim 100\%$  and  $\sim 1\%$ , respectively. They are characterised by crater formation in solid density catchers and track formation in low-density catchers. Higher shock pressures and moderate temperatures are prevalent during crater formation processes, compared to moderate shock pressures and significantly higher temperatures during track formation [61–67]. Theoretical models of hypervelocity impacts into both types of media can be found in references [61, 62, 64, 68–72], respectively. These give a good sense of the relevant physics but are not directly applicable to the warm dense plasma cloud of partially ionised matter impacting at higher velocities and temperatures into our various catcher systems. High-speed recordings of the ejecta clouds into vacuum or into various catcher systems were collected to improve the understanding of cloud dynamics and its high-speed impact.

### 3.3. High speed recordings

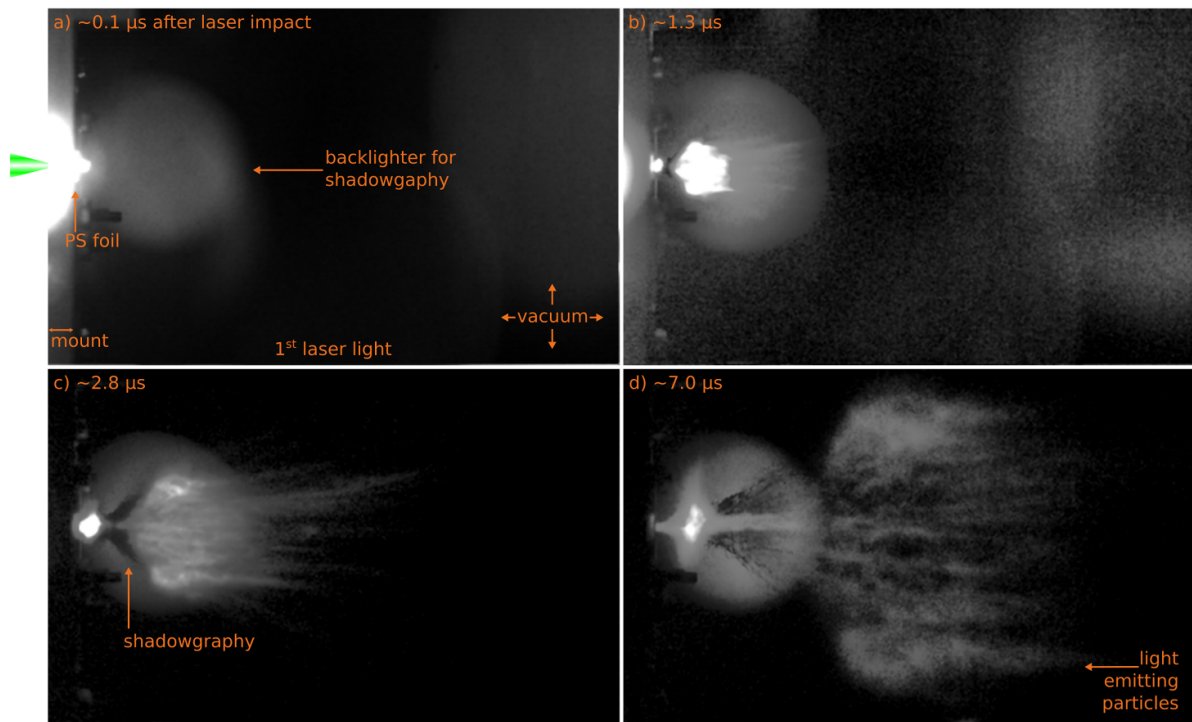
All high speed recordings presented in the following can be found in the graphics interchange format (gif) as supplementary

data files. A feasibility study at the ID19 beamline at the ESRF was performed on PG targets shock-compressed with a 5-J pump laser (Titan6, Amplitude Tech.,  $\lambda = 532$  nm, pulse length of 5 ns, laser spot size  $\sim 200 \mu\text{m}$ ) up to 50 GPa pressures. This compact experimental set-up can also be realised in small-scale laboratories. High-speed optical recordings revealed particle trajectories (see figure 3(c)) of reflection at the front surface of the aerogel and curved ones that may be particles moving along the quartz cylinder's inner wall. Some particles even did escape the catcher between the tube and plate. The observed trajectories more likely originate from the objects moving in the gap between the aerogel and the quartz cylinder (see figure 3(a)) than particles impacting into the aerogel. Future experiments should eliminate this ambiguity.

Single pictures of high-speed videos recorded with the Shimadzu Hyper Vision HPV-X2 camera with frame rates up to 10 Mfps, thus 100 ns between frames, during an experiment at the Z6 endstation at GSI Helmholtzzentrum für Schwerionenforschung GmbH are presented in figures 4 and 5 for PS and PG targets, respectively. A MHz-backlighter allows for shadowgraphy to observe particles that are not emitting light. Bright, dark, and again light-emitting particles are observable in the scenario of a freely evolving ejecta cloud into vacuum (figures 4(a)–(d)). The diamond particles are generated in the shock front of single-shocked and during the overlap of the two shock waves on the target rear side of double-shocked materials, where a quasi-steady state of the highest pressure and temperature conditions is achieved for hundreds of picoseconds presumably yielding bright particles with highest kinetic energies. Therefore, it is believed that the leading bright objects are the most compressed and fastest ones that contain

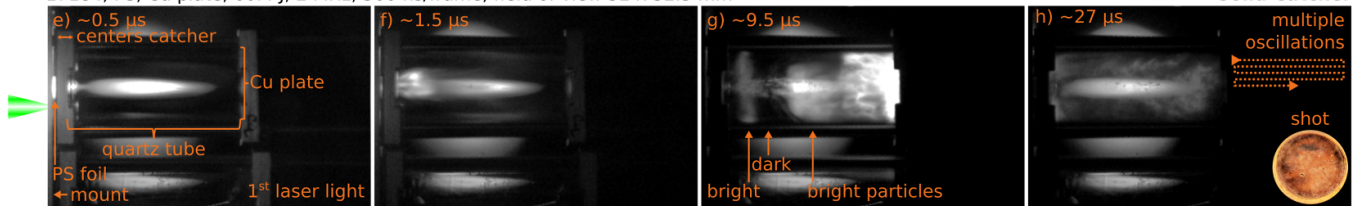
17039, PS, VISAR, 72.1 J, 10 MHz, 100 ns/frame, field of view 92 x 57.5 mm<sup>2</sup>

Freely Evolving



17184, PS, Cu plate, 60.4 J, 2 MHz, 500 ns/frame, field of view 52 x 32.5 mm<sup>2</sup>

Solid Catcher



17104, PS, SiO<sub>2</sub> 90 mg/cc, 81.7 J, 1.428 MHz, 700 ns/frame, field of view 52 x 32.5 mm<sup>2</sup>

Aerogel Catcher

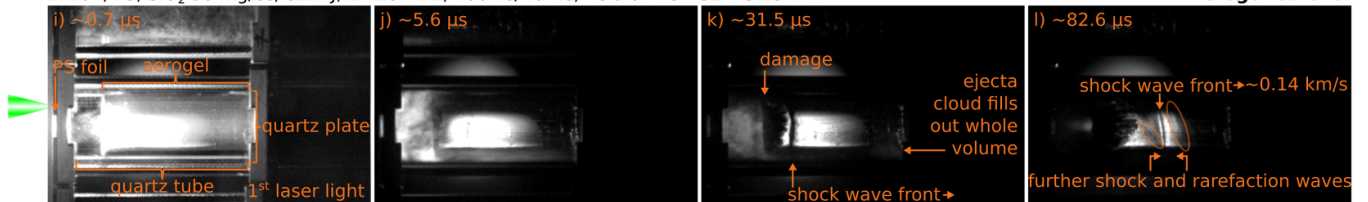


**Figure 4.** High-speed recording frames from laser shock-loaded polystyrene targets showing the evolution of the ejecta cloud after shock breakout into various environments. Reproduced from [33]. [CC BY 4.0](https://creativecommons.org/licenses/by/4.0/). (a)–(d) Dynamics when evolving into vacuum, (e)–(h) into the confined space of a solid catcher composed of a quartz tube closed by a pure copper plate of 14 mm diameter ((h) inset), and (i)–(l) into a SiO<sub>2</sub> aerogel with density of 90 mg cc<sup>-1</sup>. Some of the images were contrast-enhanced using the Fiji plugin Enhance Local Contrast (CLAHE) [75].

the diamond particles. The dark objects may be attributed to material surrounding the laser-irradiated area and being subject to pressure and temperature gradients not high enough for light emission. Finally, the bright plasma, making up the tail of the cloud, is associated with the target front surface that directly interacted with the laser pulse. Substantial differences in the cloud dynamics between the target types are observable. While the PS dynamics can be described by an expanding, funnel-like cloud moving away from the point of ejection (see figures 4(a)–(d)) with an average opening angle of  $\sim 65^\circ$  (see figure 16(a)), the PG cloud is much more directed and of elongated shape (see figures 5(a)–(d)) with an average opening angle

of  $\sim 33^\circ$  (see figure 16(b)). Identifying and tracking bright features of the cloud during their gradual darkening provided very rough estimates of maximum velocities of  $\sim 13\text{--}17\text{ km s}^{-1}$  for PS (see figures 4(a) and (b)) and  $\sim 16\text{ km s}^{-1}$  for PG (see figures 5(a) and (b)). More reliable maximum ejection velocities were deduced from a slice through a 3D-rendered volume with the recorded frames representing the dimensions  $x$  and  $y$  and the third dimension being time, which consists of the time-resolved sequence of images (see figures 17(b) and (f)). Free-surface ejection velocities between 0.4 and 12.6 km s<sup>-1</sup> for PS and between 0.2 and 26.4 km s<sup>-1</sup> for PG were observed in these specific slices.

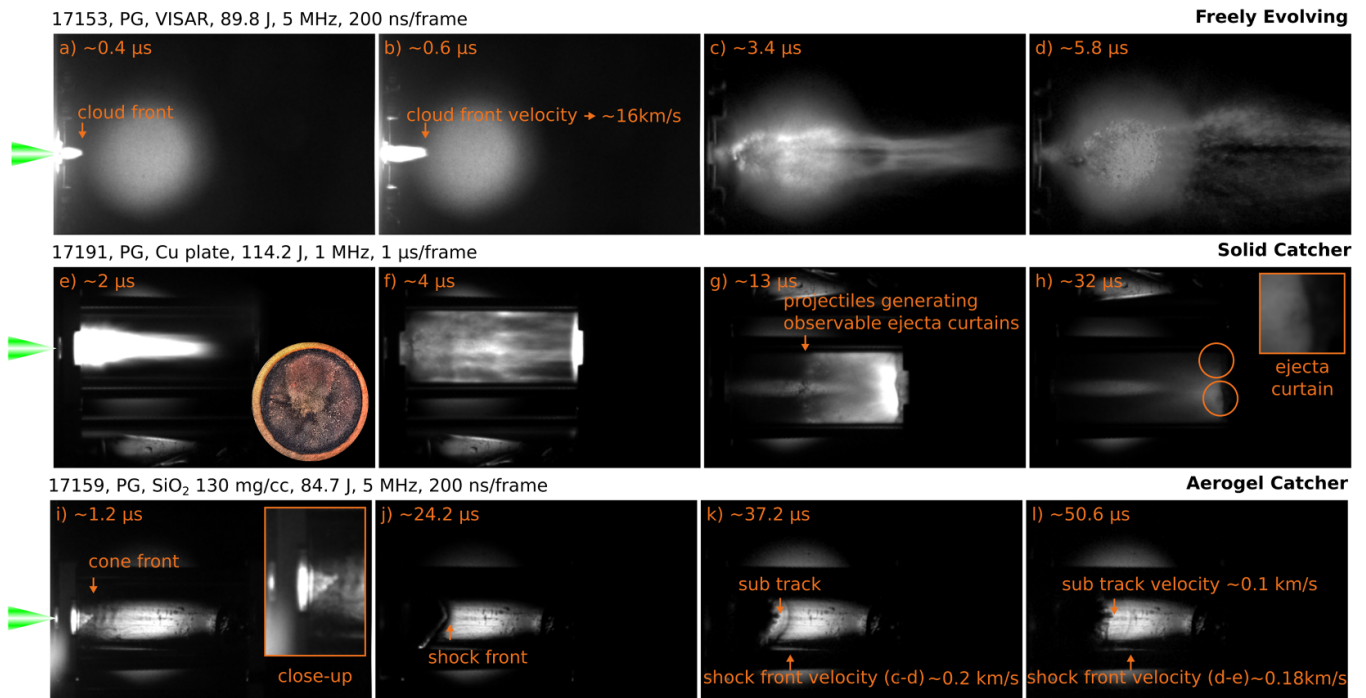


**Figure 5.** Ejecta cloud evolution after shock breakout from pyrolytic graphite targets. Reproduced from [33]. **CC BY 4.0.** (a)–(d) Freely evolving ejecta cloud into vacuum. (e)–(h) Evolution of ejecta cloud in the confined space of a quartz tube closed by a highly pure copper plate of 14 mm diameter ((e) inset). (i)–(l) Evolution of ejecta cloud in a quartz cylinder holding an SiO<sub>2</sub> aerogel of 130 mg cc<sup>-1</sup> density. Each image has a field of view of 52 × 32.5 mm<sup>2</sup>. Some of the images were contrast-enhanced using the Fiji plugin Enhance Local Contrast (CLAHE) [75].

Footage of solid catchers highlight the distortive effect of light refraction on the cylindrical quartz tubes (see figures 4(e) and 5(e)), which may be diminished using other geometries in future experiments. Particles being part of the outer plasma cloud collide obliquely with the quartz tube before hitting the metal catcher plate (see figures 4(g) and 5(f)). Oblique impacts are generally known for a more benign deceleration [74], which is beneficial for diamond preservation. The plasma cloud gathers at one end of the catcher and is reflected back performing multiple oscillations in the confined space (see figure 18(a)), while some material escapes through the hole in the target. Ejecta curtains were observable in the case of shock-compressed PG (see figure 5(h)).

The impact into the SiO<sub>2</sub> aerogel leads to clear damage on the front surface of the aerogel rendering that part opaque. The tracks emerging from the damaged areas are more pronounced in PG relative to PS samples (compare figures 4(k) and (l) with figures 5(k) and (l)). Moreover, a shock wave is overtaking the growing damage. Constituents of the warm dense plasma cloud impact the catcher rather as a collective body instead of multiple single particles over a prolonged time of tens of  $\mu$ s. Not only one but multiple shock waves are launched into the aerogel, as the plasma cloud oscillating in the confined space impacts repeatedly. Those shock waves interact with rarefactions waves from various origins and eventually lead to aerogel failure by breaking into numerous parts. This complete failure can be mitigated by using a so-called witness plate in front of the aerogel with a hole in the centre filtering out the majority of the plasma cloud (see figures 15(i)–(l)). A big advantage

is the localised spot for post analysis where the contamination with the not light emitting parts of the plasma cloud is minimised. On the other hand, the already small amount of shock-compressed material containing diamond particles may be further reduced as well.

The plasma cloud may possess the ability of self-shielding a part of itself upon impact in a confined space (compare [71]), as corroborated by high-speed recordings (see figures 4, 5, 15 and 18), in which multiple oscillations of the cloud were observable. This means that particles on the forefront of the plasma cloud are subject to the harshest impact conditions while they shield following particles. A maximum impact velocity ( $\sim 13$  km s<sup>-1</sup>) and a shock wave velocity in the aerogel ( $\sim 0.14$  km s<sup>-1</sup>) can be estimated from the high-speed recordings (see figures 4(i)–(l)). Nonetheless, the impedance mismatch technique for peak shock pressure estimation cannot be applied due to the poorly defined projectile of a spatially extended, time varying plasma cloud.

### 3.4. Raman spectroscopy

A quartz catcher plate that collected PS ejecta was investigated using Raman spectroscopy with an excitation wavelength of 473 nm (see figure 6). Sub-image 6(b) shows that the quartz plate broke into two pieces upon the force load it was exposed to. An optical microscopy image (c) illustrates the impact signs in form of finely dispersed dark spots, presumably craters, and puddles of melt. White numbers indicate the measurement locations for the Raman spectra illustrated in (e). A typical

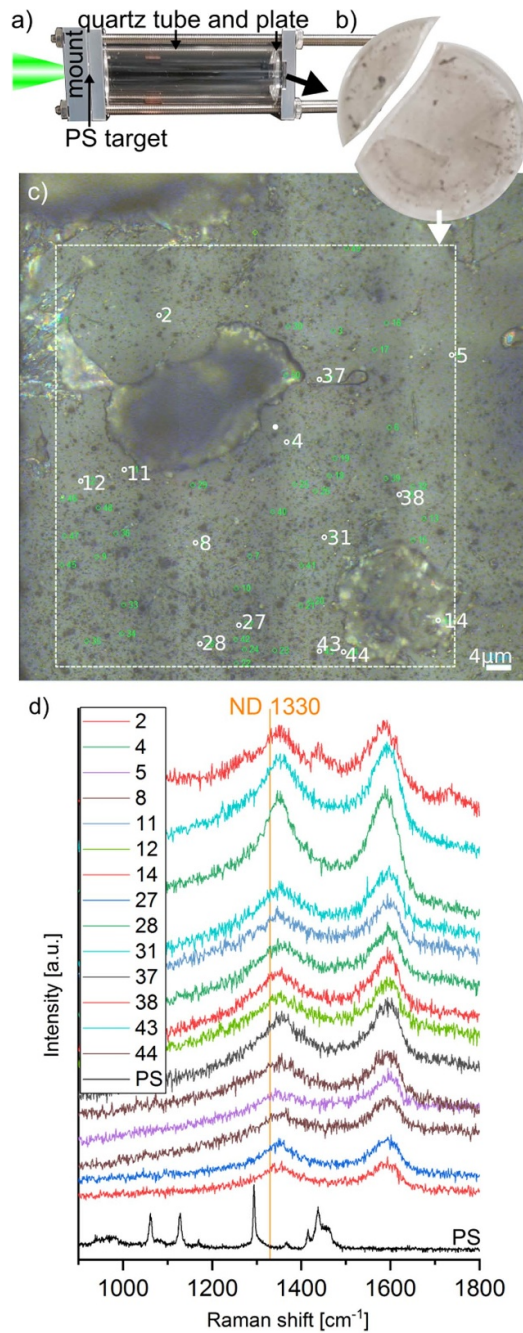


**Figure 6.** Raman spectra recorded with an excitation wavelength of 473 nm on a quartz plate of a solid catcher exposed to the free-surface release cloud of shock-compressed PS at GSI. Reproduced from [33]. [CC BY 4.0](#). (a) Side view of solid catcher made out of quartz. (b) Catcher plate broken in two parts during the capture process. (c), (d) Optical microscope image of recovered quartz catcher plate highlighting the measurement locations with white numbers for the various Raman spectra recorded. The position of the diamond line is highlighted by an orange vertical line.

broad signature of graphite D and G bands is observable around 1350 and 1580  $\text{cm}^{-1}$  [76]. The pristine PS foil does not have peaks in the vicinity of the expected diamond peak around 1330  $\text{cm}^{-1}$  [77, 78], which is marked by an orange vertical line. These Raman data are representative for multiple samples investigated by this technique. The presence of a

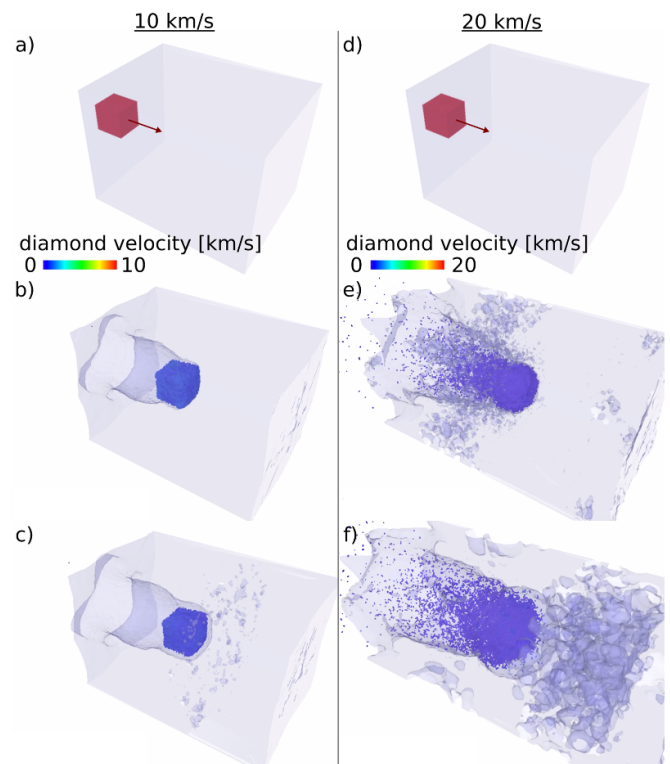


**Figure 7.** MD simulations modelling the impact of a  $\sim 6$  nm diamond cube impacting at 10  $\text{km s}^{-1}$  (a)–(c) and 20  $\text{km s}^{-1}$  (d)–(f) into a 40 nm long block of aluminium consisting of  $\sim 10^6$  atoms. Reproduced from [33]. [CC BY 4.0](#).

small shoulder at the diamond line around 1330  $\text{cm}^{-1}$  in multiple spectra is ambiguous and thus not significant. However, the transformation of PS into graphite is clearly observable. It was frequently observed that the diamond particles are encapsulated by a graphitic shell during the synthesis of detonation nanodiamonds [79, 80]. We think that we observe this process in our experiments as well. In fact, it is most likely that the diamond surfaces exhibit a graphitic reconstruction due to the release into vacuum or they may be hydrogenated due to the presence of hydrogen in our PS samples. In case of graphitic envelopes around nanodiamonds, a very high diamond content ( $\gtrsim 70\%$  at 325 nm  $\lambda$  [80]) is necessary to distinguish the diamond signal among the  $\text{sp}^2$  signal, which is not expected. Future analysis with an excitation wavelength in the UV spectral region is planned in order to give a better balanced Raman cross-section between  $\text{sp}^2$  and  $\text{sp}^3$  carbon [81, 82], a shallower sampling depth [83], and significantly less photoluminescence background [84, 85]. Moreover, a future, thorough campaign of selective oxidation [79] aiming at diminishing the graphitic shell may be able to confirm the presence of a diamond core for our samples.

### 3.5. MD simulations: impact scenarios

The MD simulations displayed in figure 7 model the impact of a diamond cube with an edge length of  $\sim 6$  nm into a block of aluminium at 10  $\text{km s}^{-1}$  (a)–(c) and 20  $\text{km s}^{-1}$  (d)–(f), respectively. The edges of the diamond cube soften but the

diamond particle stays mostly intact in the  $10 \text{ km s}^{-1}$  scenario. Additionally, voids appear in deeper regions below the impact crater. Large parts of the diamond cube and the aluminium block evaporate in the  $20 \text{ km s}^{-1}$  scenario. Interestingly, there are no major differences in the simulation results at this microscopic scale compared to typical simulations on the macroscopic scale predicting a negligible role of the size effect in such kind of hypervelocity impacts. The simulations indicate that the diamond cube penetrates into the solid catcher material and may still be found at the deepest point of the crater. Lower impact velocity simulations yielding much shallower craters predict a projectile recoil at  $4 \text{ km s}^{-1}$  (not presented here) such that the nanodiamond is released into the confined space of the catcher and may be eventually found on the catcher plate's surface. Such a scenario is realistic considering the self-shielding properties of the plasma cloud.

### 3.6. Electron microscopy

Distances between target and catcher plate (12 to several tens of millimetres) and the diameter of the plate (5–14 mm) vary among and within experiments. The influence of the former is expected to play a non-negligible role for recovery with respect to the amount of time for the shock-compressed material to relax and potentially stabilise before impact. This results in more or less scattered impact sites. Therefore, volumetric analysis techniques applied, like x-ray diffraction, did not yield promising outcomes. Hence, techniques analysing localised sites appear to be the more promising ones.

Scanning electron microscopy (SEM) images of pristine catcher plates, i.e. contamination control samples (CCS), are compared to representative SEM data of catcher plates exposed to either shock-compressed PS or PG in figure 8. The detected spherical-like objects in pristine and recovered samples were found to differ substantially with respect to their size and morphology. The ones on the pristine catcher plates (a)–(d) are in the tens of nanometre range in comparison with spherical-like particles in the size range of up to hundreds of nanometres detected on the recovery samples. The size distributions of spherical-like objects on PS and PG recovery samples are similar. Apart from isolated spherical-like objects on PS (e) and PG recovery samples (g), objects encapsulated in material (f) and particles exhibiting signs of edges and vertices (h) are predominant. The objects' surfaces are smooth (e) or textured (g) and in some cases have a facet-like appearance (h). Furthermore, craters (g), loose material (e)–(h) and string-like (f) structures are present.

Energy-dispersive x-ray spectroscopy (EDX) measurements on the spherical-like objects' sites estimate a significantly high carbon content  $\gtrsim 50 \text{ at.}\%$  on a PS and a PG recovery sample (see figure 9) where the probing depth, however, clearly exceeds the average diameter of these object types. Thus, neglecting the H content which is not accessible by EDX analysis, the spherical-like particles are to a large part or potentially even completely composed of carbon (a)–(d), and there is a thin carbon-based coating on the catcher plate (e), (f) deduced from a measurement site next to the spherical-like object. These objects are potential diamond candidates.

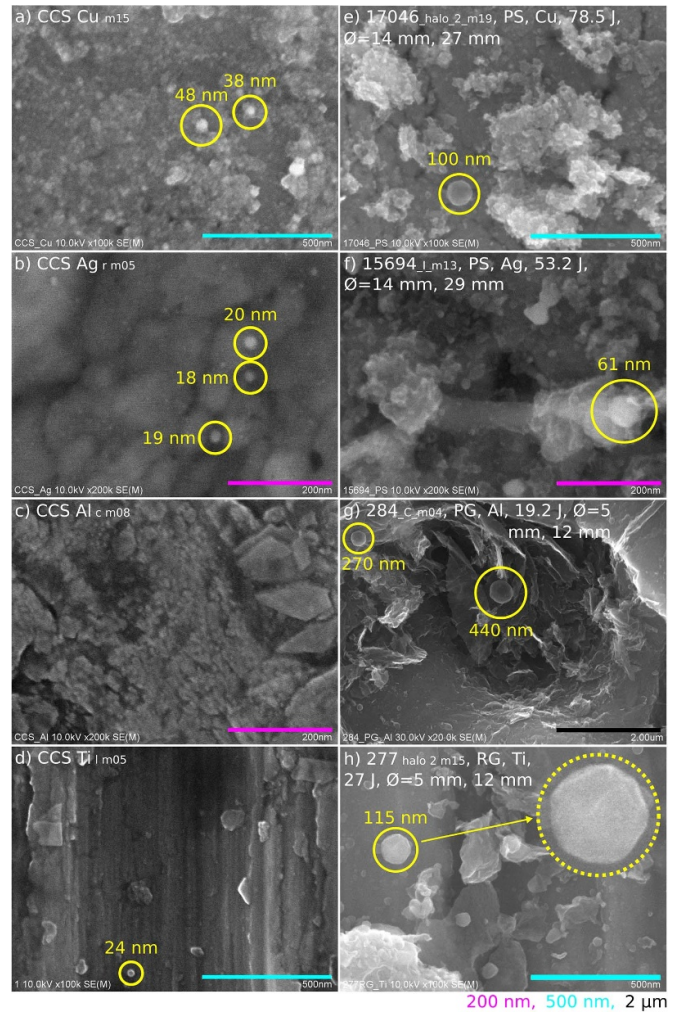


**Figure 8.** SEM images of different types of pristine solid catcher plates that serve as contamination control samples (CCS, 1st column): (a) copper, (b) silver, (c) aluminium, (d) titanium. Reproduced from [33]. CC BY 4.0. The 2nd column shows the corresponding recovered catcher plates that were exposed to either shock-compressed PS or PG. The label displays the sample ID, target and catcher material, the laser energy of the shot as well as the catcher plate's diameter and its distance from the target. Some images were contrast-enhanced using the Fiji plugin Enhance Local Contrast (CLAHE) [75].

Surface-sensitive Auger electron spectroscopy (AES) data from a Ti catcher plate that was exposed to shock-compressed rigid graphite (RG) (see figure 10) with an information depth of  $\sim 5 \text{ nm}$  confirm that not only the spherical-like object but also its vicinity contains an at least  $\sim 5 \text{ nm}$  thick carbon layer. Typically, a natural contamination layer of hydrocarbons on air-exposed surfaces is a few nanometres (2–4 nm) thick [86] and needs to be taken into account. All three measurement sites showed a strong signature of carbon around 268 eV arising from the KLL transition [87, 88] and a small feature around 510 eV attributed to oxygen superimposed on a background intensity increasing with kinetic energy (see figure 19). Reference spectra of highly oriented PG (HOPG) and diamond were recorded and compared to the sample data (see figure 10(b)). It is evident that distinguishing between carbon allotropes using

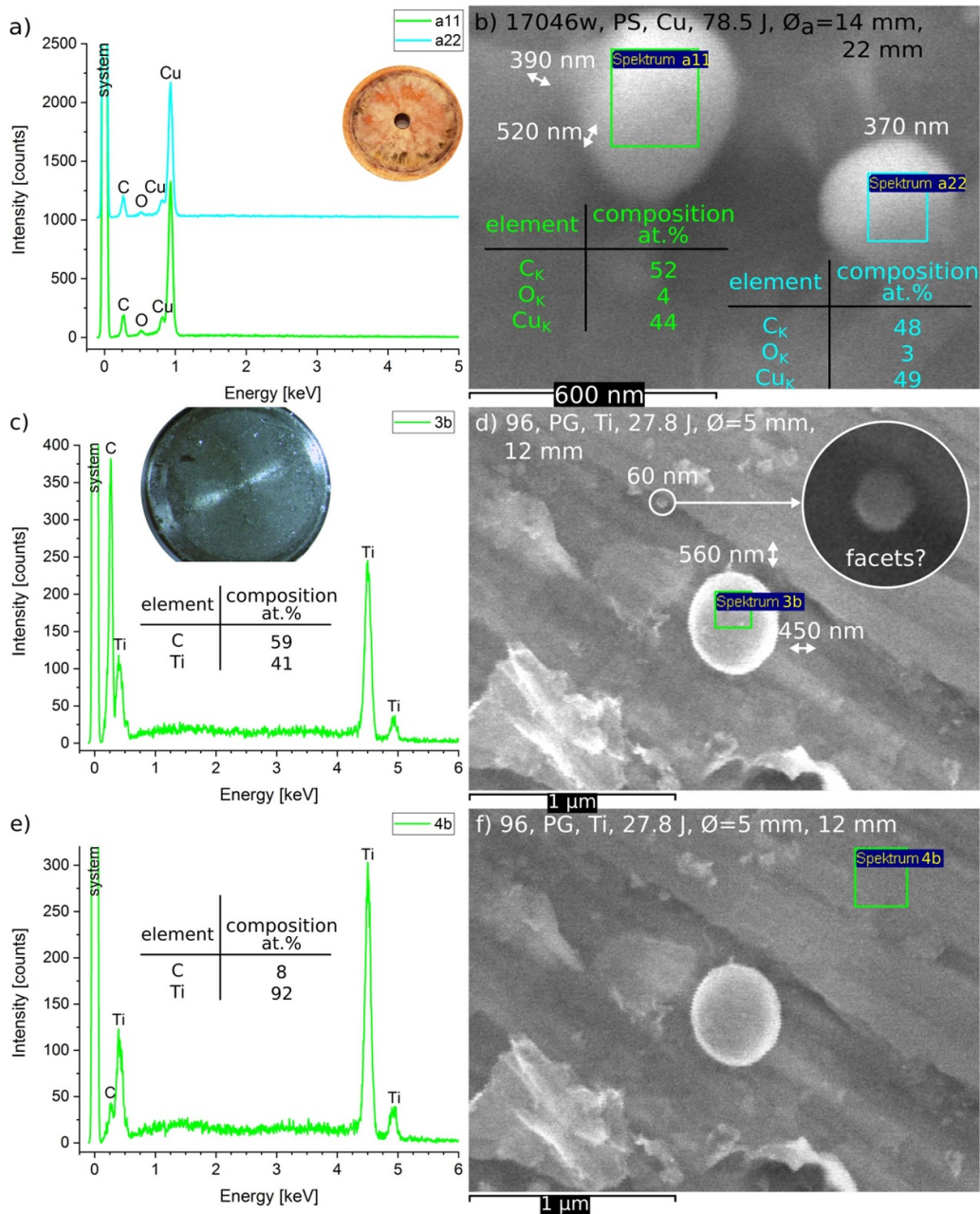


**Figure 9.** Element analysis using energy-dispersive x-ray spectroscopy (EDX) of two recovery samples: (a), (b) two spherical-like objects on a 14 mm Cu witness plate that collected shock-compressed PS; (c), (d) a spherical-like object on a 5 mm Ti catcher plate that was exposed to shock-compressed PG; (e), (f) a site on the Ti catcher that collected shock-compressed PG in the vicinity of the spherical-like object. Reproduced from [33]. CC BY 4.0. Each row shows the EDX spectra, tables with rough estimations of the atom percentage of the respective elements detected and the corresponding measurement sites in an SEM image.

AES is challenging due to only subtle changes in the spectrum. The most prominent differences are the shoulder in the HOPG spectrum around 255 eV, while the diamond spectra tend to peak at higher kinetic energies. However, most of this shift in the peak position can be attributed to charging effects, as can be seen from the dependence of the peak position on the probing electron beam current. Extrapolating the peak positions to 0 A electron beam current yields a peak shift of only about 2 eV in comparison to the HOPG data. A shoulder is present in the sample data, indicating the presence of graphitic material, which may be a graphitic shell around a diamond core [79].

Spherical-like objects can either be projectiles composed of target material formed in the laser shock-loaded target, or they can condense in the vapour expansion or excavation stage of crater formation in response to the high-speed impact [62], in which case they can consist of either catcher only (projectile stays intact) or catcher and target material. With these objects being potential diamond candidates, TEM lamella cross-sections of three different spherical-like objects were prepared by focused ion beam (FIB) cutting and subsequently investigated with respect to their element composition (see figures 11–13) and in one case structure (see figure 14).

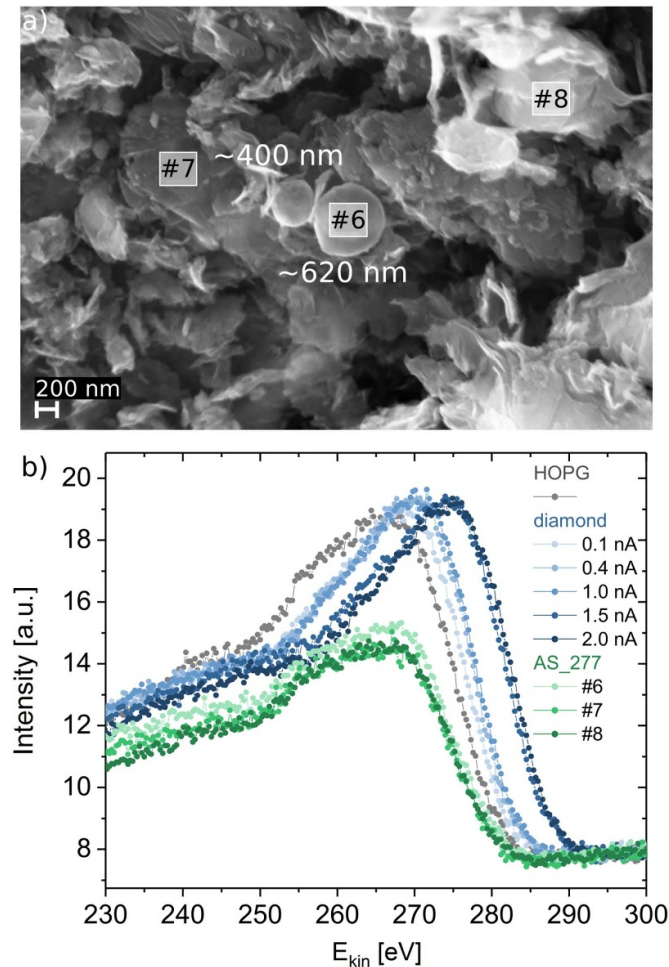


**Figure 10.** Auger electron spectroscopy (AES) analysis of sample 277, rigid graphite (RG), Ti catcher plate, 27 J. (a) SEM image displaying the AES measurement locations. Reproduced from [33]. [CC BY 4.0](#). (b) Comparison of sample spectra with recorded reference data of highly oriented pyrolytic graphite (HOPG) and diamond.

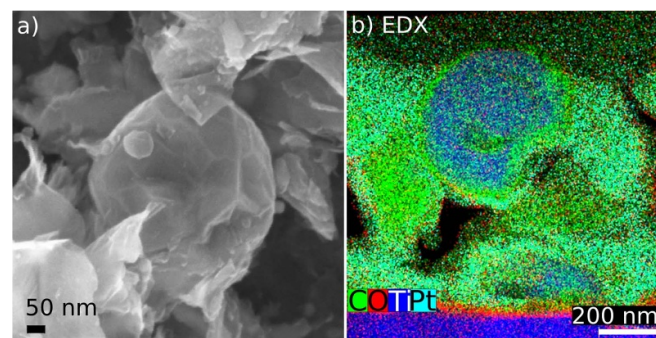


**Figure 11.** (a) Top-view SEM image, and (b) cross-sectional, spatially-resolved EDX data obtained in scanning TEM mode for sample 277, RG, Ti, 27 J. Reproduced from [33]. [CC BY 4.0](#).

TEM lamellae were prepared by *in situ* lift-out using a Zeiss Crossbeam NVision 40 system. A platinum cap layer for protection of the object of interest was deposited beginning with electron-beam-assisted and subsequently by Ga-focused-ion-beam-assisted precursor decomposition. In the following, the lamellae were prepared using a 30 keV Ga FIB with adapted currents and were transferred to a lift-out grid using a

micromanipulator. Ga ions with only 5 keV were used for final thinning of the TEM lamellae to electron transparency (thickness  $\sim 100$  nm) to minimise sidewall damage.

The three different types of spherical-like objects are categorised into the three compositional groups: (1) a mixture of target and catcher material (C, Ti; see figure 11(b)), (2) catcher material (Al, O on the particle's surface; see figure 12(b)),

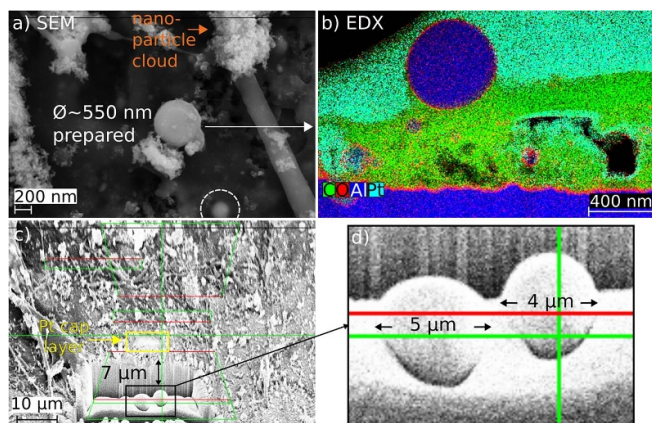


**Figure 12.** The 550 nm sized spherical-like object (a) originates from sample 158, PS, Al, 45 J. Reproduced from [33]. CC BY 4.0. Cross-sectional, spatially-resolved EDX data obtained in scanning TEM mode are illustrated in sub-image (b). An interim image recorded during the Ga-FIB-based TEM lamella preparation process is shown in (c) with green and red auxiliary lines. Buried spherical-like objects were observed 7  $\mu\text{m}$  below the catcher's surface, that showed higher resistance to the FIB than the surrounding material, but eventually disappeared. A close-up of these objects is shown in sub-image (d). Contrast enhancement with the Fiji plugin Enhance Local Contrast (CLAHE) [75] was used for the sub-images (a), (c), (d). While spherical-like objects are promising diamond candidates, a second type of diamond candidate is additionally shown in sub-image (a), namely a collection of nm-sized particles highlighted by an orange arrow. The dashed white circle in sub-image (a) marks another not further analysed spherical-like object.

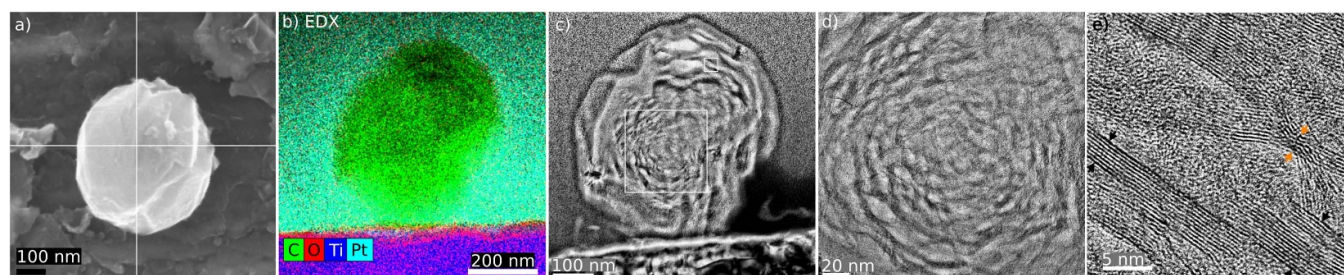


**Figure 13.** (a) Top-view SEM image with white auxiliary lines, (b) cross-sectional, spatially-resolved EDX data obtained in scanning TEM mode, and (c), (d) corresponding bright-field and (e) high-resolution TEM images of sample 277, RG, Ti, 27 J. Reproduced from [33]. CC BY 4.0. The close-ups (d) and (e) show the central and outer region of the spherical-like object, respectively. The region locations are indicated by white squares in (c). Contrast enhancement with the Fiji plugin Enhance Local Contrast (CLAHE) [75] was used for the sub-images (a), (c), (d), (e).

and (3) target material (C; see figure 13(b)). A possible explanation of the first case (see figure 11) is that projectile and catcher melted during impact, followed by their mixture and ejection during the crater formation process, serving as a source for spherical-like particle formation. In the second case (see figure 12), it is possible that the projectile, potentially diamond, stayed intact when the catcher material melted and was emitted as ejecta curtain from which spherical-like objects formed.

In the last scenario of the RG recovery sample (see figure 13), the object may once have been a diamond particle that transformed upon impact into a shell-like graphitic structure with increasing voids towards its outer parts (see figure 13). Neatly ordered, stacked carbon lattice planes form ribbons ((d), (e) marked by black arrows) that can twist ((d), (e) orange arrows). Structural analysis of the central part of this object was performed using selected area electron diffraction (SAED) (see figure 14). Sub-image (b) shows the diffraction raw data, while sub-image (c) and (d) additionally present

an overlay with simulated diffraction ring positions of diamond and graphite, respectively. The corresponding line-out was obtained via azimuthal integration using the Fiji plugin polar transformer [89] (e). The presented data show no conclusive evidence for the presence of a diamond phase. However, there is a good match between the sample data and the simulated in-plane Bragg peaks of graphite, 100 and 110. The positions of the 002 and 004 reflections are shifted towards lower Q values indicating larger distances in the c-direction (i.e. distances between the graphene sheets) than expected. The interpretation of this object being a diamond before impact would agree with reports from two-stage light gas gun experiments in which diamond projectiles (0.3–0.5 mm) were accelerated between 2.75 and 6  $\text{km s}^{-1}$  into an aluminium plate [90, 91] predicting an upper preservation limit at 4.3  $\text{km s}^{-1}$  ( $\hat{=}$  60 GPa), while at higher impact velocities melt features were observed and various forms of poorly crystallised graphite were detected. On the other hand, Bunch *et al* report that this interpretation is based on surface-sensitive

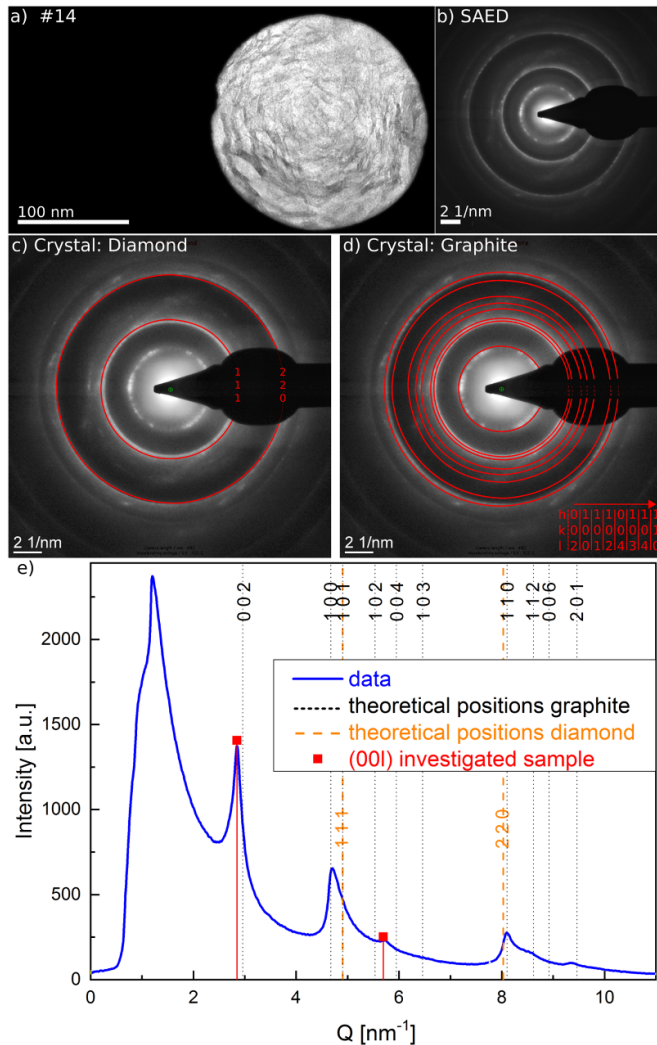


**Figure 14.** Selected-area electron diffraction (SAED) pattern (b) of the area presented in the cross-sectional TEM image (a) and overlaid with the expected diffraction rings for diamond ((c), JCPDS database number 6-675) and graphite ((d), JCPDS database number 41-1487) of the spherical-like object on sample 277, RG, Ti, 27 J, (see figure 13, in particular sub-image (c)). Reproduced from [33]. CC BY 4.0. The corresponding lineout (e) was obtained via azimuthal integration and is compared to the simulated positions of the graphite and diamond Bragg peaks.

analysis techniques, such that the notion of diamond being buried under the residue surface cannot be excluded [90]. The latter is also corroborated by our MD simulations.

Interestingly, three spherical-like particles (see two of them in figures 12(c) and (d)) with a few  $\mu\text{m}$  diameters were detected about  $7\ \mu\text{m}$  underneath the catcher plate's surface in the course of TEM lamella preparation of a PS recovery sample on an aluminium plate. They showed a higher resistance to the Ga FIB than the surrounding material. They were not further analysed since this would have required the loss of the initially aspired TEM lamella of the  $550\ \text{nm}$  spherical-like object on the surface of the catcher plate (see figure 12(a)). Therefore, it can only be speculated whether they were buried diamond particles [90]. Surprisingly, no craters were visible leading to

these objects. A potential explanation is that the head of the plasma cloud melted the aluminium surface ( $T_{\text{melt}}^{\text{Al}} = 660\ ^\circ\text{C}$  [92]) such that subsequently impacting projectiles faced a liquid instead of a solid-state catcher. Besides, a second type of diamond candidate is visible in figure 12(a) (orange arrow). It strongly resembles nanodiamonds from laser-assisted techniques namely light hydro-dynamic pulse synthesis with its appearance of a cloud made from nm particles (compare to [93] figures 5.2(a), (d) and [94] figure 2). Investigation of such a particle cloud with a UV Raman instrument featuring an appropriate small probing spot is envisioned in the future.

#### 4. Conclusion and outlook

The formation of diamond particles in laser shock-loaded graphite and hydrocarbon targets was demonstrated in previous experiments by *in situ* XRD data at the moment of their creation [12, 13, 19]. They are assumed to be preserved during their free expansion from extreme pressure and temperature conditions based on indicative MD simulation predictions and *in situ* XRD data recorded several nanoseconds after shock breakout. Such XRD measurements are planned to be verified in future experiments. That data will additionally be able to determine whether the diamond particles keep growing after the shock release within the ejecta cloud. High-speed videos revealed that this cloud oscillates multiple times back and forth in the confined catcher space instead of being forced to a halt upon first impact highlighting the cloud's self-shielding properties. It is a poorly defined impactor especially in the warm dense matter regime, where no theoretical predictions have been made to date according to the knowledge of the authors.

Raman measurements of catcher plates in the more suitable UV spectral region may be able to already answer the question of whether diamonds have been recovered. Until now, only the transformation of PS to graphite can be claimed with certainty from the recovered and analysed samples. The hypothesis that the graphite signals may arise from a graphitic shell around a diamond core [79, 80] can be tested in future selective oxidation campaigns.

All combinations of target (PS, PG) and catcher (solid, aerogel, others) exhibited spherical-like objects which are promising diamond candidates. To date, only three such objects out of numerous ones were analysed more closely. They all significantly differed in their chemical composition and structure. An elaborate investigative campaign is necessary to find further types of objects and to collect statistically relevant data. Moreover, it is possible and likely that diamond particles are indeed buried in the catcher plates [90], since buried spherical-like particles were detected in our recovery samples but they were not yet further analysed.

The data presented here are the most promising findings obtained so far. In the following, further work already performed in the framework of this project is briefly mentioned without details. Ongoing investigations have been focusing on aerogel catchers, which are much more difficult to analyse

and often require prior chemical preparation. A concentration technique of material deposits found on the inner wall of the catcher quartz tube was developed using small amounts of either deionised water or analytical-grade alcohol in combination with an ultrasonic bath. Moreover, electrolysis using catcher plates as electrodes was found to have potential to bring the diamond particles in solution, potentially also the buried ones. A detailed and complete report about this project in this emerging research field can be found in [33]. In upcoming recovery experiments, other type of hydrocarbon targets with various C–H–O stoichiometry will be used in combination with newly developed catcher designs based on the experience gained.

A solid foundation towards successful recovery of diamond and lonsdaleite in the high-pressure regime using laser-induced shock compression based on the example of graphite and PS samples was established. Its prospects with respect to PS are rich in terms of potentially providing insights in the diamond formation process that is relevant for interior models of Uranus, Neptune, and comparable planets [12–14]. Ever-increasing laser energies and repetition rates may render the here presented technique to a tailorable diamond production method as an alternative to already established production routes [95] in the far future. Currently, we are taking the first steps towards this goal. In particular, the notion of generating doped diamond particles with enhanced properties [46] by using doped targets or certain type of catcher materials is encouraging. In general, exotic structures equipping elements with new behaviour may be found and recovered by exploring the phase diagram of matter. This is possible thanks to the continuous progress in laser technology fostering new applications. With that, this long-standing goal of condensed matter physics may potentially soon be reached. Moreover, recovery may become an additional diagnostic in pump-probe experiments in the future being able to fortify the observed *in situ* data.

## Data availability statement

The data that support the findings of this study are available upon reasonable request from the authors.

## Acknowledgments

The authors want to express their gratitude to M Sobiella, F Donat, H Gude R Schönert, R Hensel, B Lange, L Heinrich, E Christalle, A Kunz, A Scholz, B Scheumann, R Aniol, W Nazarov, L Bischoff, A Blazevic, U Eisenbarth, S Götte, S Kunzer, Zsuzanna Slattery-Major, B Zielbauer, and D Chorvát for their support in the preparation and performance of experiments and post-analysis of the collected samples and data.

A K S, K V, J L and D K are fully and N J H in part supported by the Helmholtz Association under VH-NG-1141. We acknowledge support by DOE FES through FWP 1001182. Support by the Structural Characterization Facilities Rossendorf at IBC and the funding of TEM Talos by the German Federal Ministry of Education and Research (BMBF), Grant No. 03SF0451, in the framework of HEMCP are acknowledged. The work of T D, A P and S Fr. was fully or in part performed under the auspices of the U.S. Department of Energy by Lawrence Livermore National Laboratory under Contract No. DE-AC52-07NA27344. This research was also supported in part by the U.S. Department of Energy, Office of Science, Office of Basic Energy Sciences, Materials Sciences and Engineering Division under Contract No. DE-AC02 05-CH11231, within the van der Waals Heterostructures Program (KCWF16), which provided for aerogel synthesis, and TEM, SEM, FTIR, and density characterization. R W F acknowledges support from the U.S. DOE, Office of Science, Fusion Energy Sciences under DE-AC02-05CH11231 and NNSA under DE-NA0003842.

Appendix

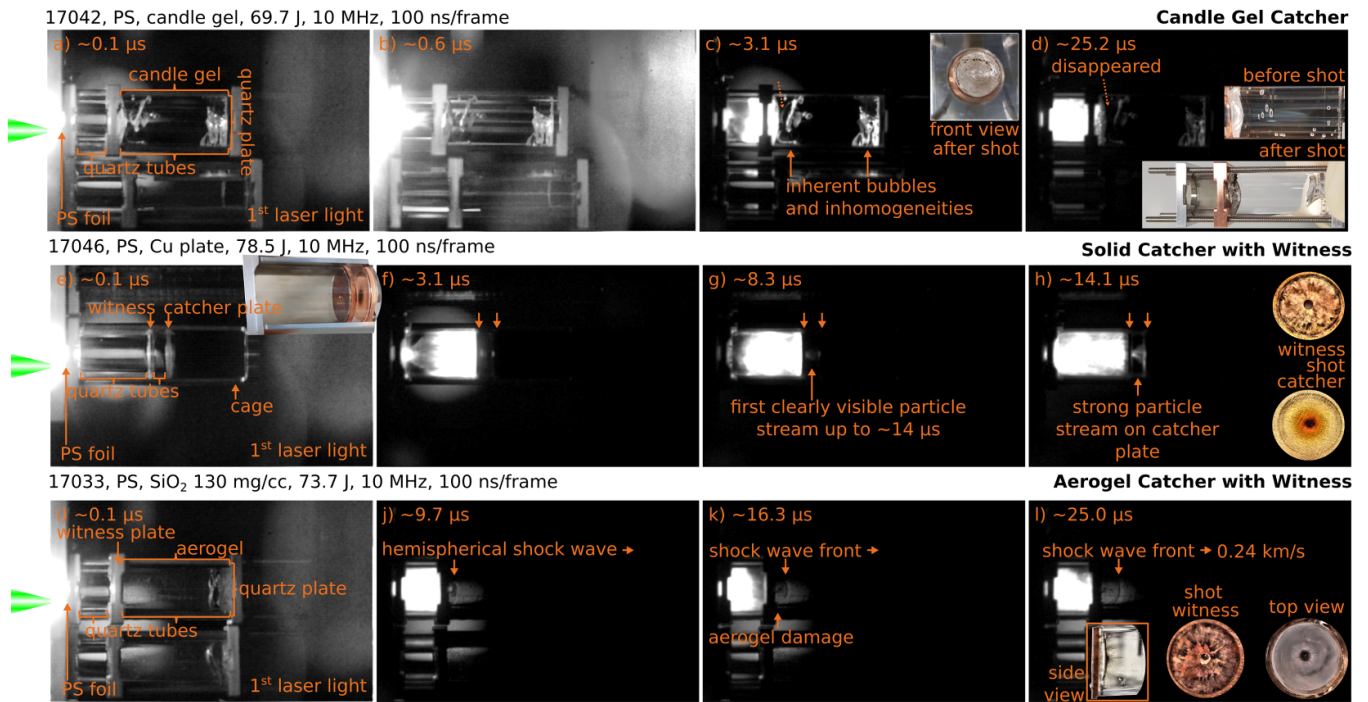


**Figure 15.** High-speed recording frames of laser shock-loaded polystyrene targets showing the evolution of the ejecta cloud after shock breakout into various environments. Reproduced from [33]. [CC BY 4.0](https://creativecommons.org/licenses/by/4.0/). (a)–(d): Into a quartz cylinder filled with organic gel of density  $820 \text{ mg cc}^{-1}$ . (e)–(h): Into a solid catcher where a witness plate made from pure copper with a hole of 1.6 mm is placed 5 mm in front of the copper catcher plate (see insets (e) and (h)). (i)–(l): Into an aerogel catcher where a copper witness plate is placed a few millimetres in front of the aerogel of density  $130 \text{ mg cc}^{-1}$ . The shot witness plate as well as side and front view of the aerogel are shown as insets in sub-image (l). Each image has a field of view of  $92 \times 57.5 \text{ mm}^2$ . Some of the images were contrast-enhanced using the Fiji plugin Enhance Local Contrast (CLAHE) [75].

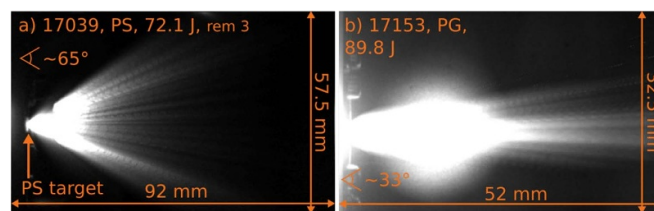


**Figure 16.** The maximum projection of a free-surface release cloud of shock-compressed polystyrene (a) was obtained using the function ‘Kymograph Evaluation’ in the Fluorescence Image Evaluation Software for Tracking and Analysis (FIESTA) [73]. Every third image of the recording in which the backlighter was visible was removed. The maximum projection of a free-surface release cloud of shock-compressed pyrolytic graphite (b) was generated using the Fiji plugin volume viewer [96]. Here the backlighter was visible in every frame. The ejection angles of the shock-compressed PS and PG clouds are  $\sim 65^\circ$  and  $\sim 33^\circ$ , respectively.

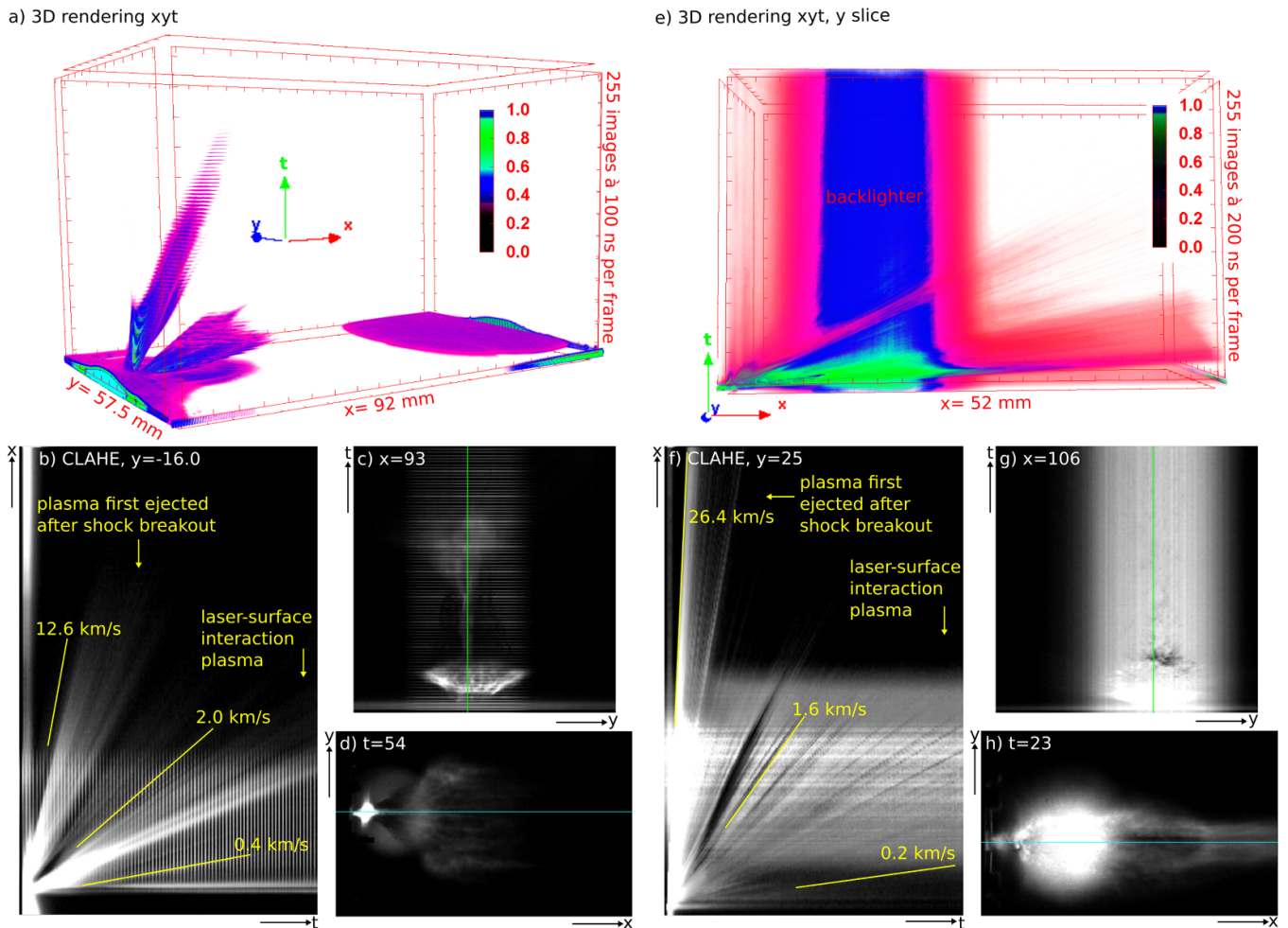


**Figure 17.** 3D-rendered high-speed video frames with the third dimension being time are generated with the Bruker software CTvox (a), (e) [97] and the Fiji plugin volume viewer (b)–(d), (f)–(h) [96]. Sub-images (a)–(d) illustrate the free-surface release of shock-compressed PS for sample 17 039, 72.1 J, 10 Mfps and (e)–(h) show the free-surface release of shock-compressed PG into vacuum for sample 17 153, 89.8 J, 5 Mfps. The green (c), (g) and blue lines (d), (h) show the slice positions of sub-images (b) and (f), respectively.

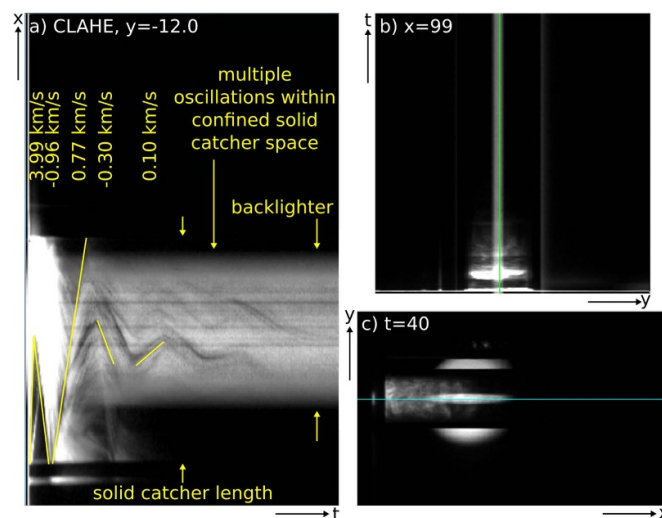


**Figure 18.** The Fiji plugin volume viewer [96] was used to obtain 3D-rendered high-speed video frames of sample 17 081, PS, Cu plate, 83.2 J, 500 kfps with the third dimension being time to deduce ejection velocities of plasma cloud features within a solid-state catcher over the course of time. The green (b) and blue line (c) show the slice positions of sub-image (a).

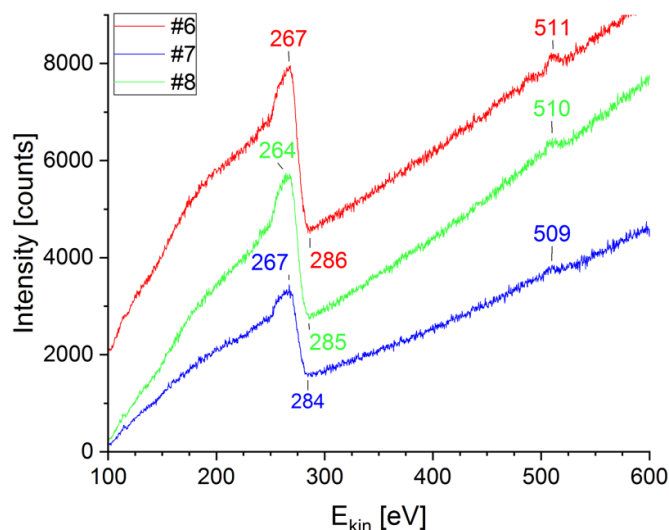


**Figure 19.** Full Auger electron spectra (AES) of sample 277, rigid graphite (RG), Ti catcher plate, 27 J (see figure 10). Reproduced from [33]. CC BY 4.0.

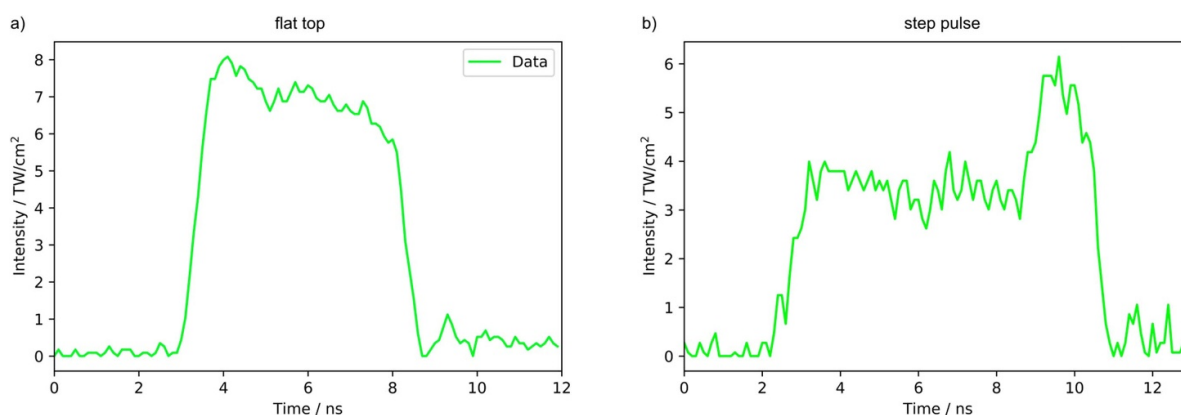


**Figure 20.** Laser pulse shapes used during experiments at GSI. The laser parameters for experiments performed at LCLS can be found in [12, 13, 19]. Reproduced from [33]. CC BY 4.0.

## ORCID iDs

A K Schuster  <https://orcid.org/0000-0001-5489-5952>  
 T Cowan  <https://orcid.org/0000-0002-5845-000X>  
 S H Glenzer  <https://orcid.org/0000-0001-9112-0558>  
 M J MacDonald  <https://orcid.org/0000-0002-6295-6978>  
 I Prencipe  <https://orcid.org/0000-0003-0931-1350>  
 A Rack  <https://orcid.org/0000-0001-9486-3621>

## References

- [1] Ramakrishna K and Vorberger J 2019 *Ab initio* dielectric response function of diamond and other relevant high pressure phases of carbon *J. Phys.: Condens. Matter* **32** 095401
- [2] Vorberger J, Plageman K U and Redmer R 2020 The structure in warm dense carbon *High Energy Density Phys.* **35** 100737
- [3] Dornheim T, Vorberger J and Bonitz M 2020 Nonlinear electronic density response in warm dense matter *Phys. Rev. Lett.* **125** 085001
- [4] Zhang S, Driver K P, Soubiran Fçois and Militzer B 2017 First-principles equation of state and shock compression predictions of warm dense hydrocarbons *Phys. Rev. E* **96** 013204
- [5] Paul Drake R 2006 Introduction to high-energy-density physics *High-Energy-Density Physics* (Berlin: Springer) pp 1–17
- [6] U.S. Department of Energy, Office of Science and National Nuclear Security Administration 2009 Basic research needs for high energy density laboratory physics (Washington, DC: U.S. Department of Energy)
- [7] Danson C, Hillier D, Hopps N and Neely D 2015 Petawatt class lasers worldwide *High Power Laser Sci. Eng.* **3** E3
- [8] Danson C N *et al* 2019 Petawatt and exawatt class lasers worldwide *High Power Laser Sci. Eng.* **7** E54
- [9] Eliezer S 2002 *The Interaction of High-Power Lasers With Plasmas* (Boca Raton, FL: CRC Press)
- [10] Eliezer S and Mima K 2008 *Applications of Laser-Plasma Interactions* (Boca Raton, FL: CRC Press)
- [11] Paul Drake R 2010 High-energy-density physics *Phys. Today* **63** 28
- [12] Kraus D *et al* 2017 Formation of diamonds in laser-compressed hydrocarbons at planetary interior conditions *Nat. Astron.* **1** 606

- [13] Kraus D *et al* 2018 High-pressure chemistry of hydrocarbons relevant to planetary interiors and inertial confinement fusion *Phys. Plasmas* **25** 056313
- [14] Schuster A K *et al* 2020 Measurement of diamond nucleation rates from hydrocarbons at conditions comparable to the interiors of icy giant planets *Phys. Rev. B* **101** 054301
- [15] Hernandez J-A *et al* 2020 Direct observation of shock-induced disordering of enstatite below the melting temperature *Geophys. Res. Lett.* **47** e2020GL088887
- [16] Morard G *et al* 2020 *In situ* x-ray diffraction of silicate liquids and glasses under dynamic and static compression to megabar pressures *Proc. Natl Acad. Sci.* **117** 11981–6
- [17] Kritcher A L *et al* 2020 A measurement of the equation of state of carbon envelopes of white dwarfs *Nature* **584** 51–54
- [18] Emma P *et al* 2010 First lasing and operation of an ångstrom-wavelength free-electron laser *Nat. Photon.* **4** 641–7
- [19] Kraus D *et al* 2016 Nanosecond formation of diamond and lonsdaleite by shock compression of graphite *Nat. Commun.* **7** 10970
- [20] McMillan P F 2002 New materials from high-pressure experiments *Nat. Mater.* **1** 19–25
- [21] Hwang H *et al* 2020 Subnanosecond phase transition dynamics in laser-shocked iron *Sci. Adv.* **6** eaaz5132
- [22] Gorman M G *et al* 2019 Recovery of metastable dense Bi synthesized by shock compression *Appl. Phys. Lett.* **114** 120601
- [23] Gorman M G *et al* 2020 Recovery of a high-pressure phase formed under laser-driven compression *Phys. Rev. B* **102** 024101
- [24] Williams C L 2019 *Structure-Property Relationships Under Extreme Dynamic Environments: Shock Recovery Experiments (Synthesis SEM Lectures on Experimental Mechanics)* vol 2 (Switzerland: Springer Nature Switzerland AG 2022) pp 1–155 (available at: <https://link.springer.com/content/pdf/bfm:978-3-031-79725-5/1>)
- [25] Boehler R 2005 Diamond cells and new materials *Mater. Today* **8** 34–42
- [26] Benedetti L R, Nguyen J H, Caldwell W A, Liu H, Kruger M and Jeanloz R 1999 Dissociation of CH<sub>4</sub> at high pressures and temperatures: diamond formation in giant planet interiors? *Science* **286** 100–2
- [27] Hörz F, Cintala M J, Zolensky M E, Bernhard R B, Haynes G, See T H, Tsou P and Brownlee D E 1998 Capture of hypervelocity particles with low-density aerogel *Technical Report* TM-98-201792
- [28] Hörz F *et al* 2006 Impact features on Stardust: implications for comet 81P/Wild 2 dust *Science* **314** 1716–19
- [29] Burchell M J, Creighton J A, Cole M J, Mann J and Kearsley A T 2001 Capture of particles in hypervelocity impacts in aerogel *Meteorit. Planet. Sci.* **36** 209–21
- [30] Lescoute E, De Ressaiguié T, Chevalier J-M, Boustie M, Cuq-Lelandais J-P and Berthe L 2009 Soft recovery technique to investigate dynamic fragmentation of laser shock-loaded metals *Appl. Phys. Lett.* **95** 211905
- [31] Lescoute E, De Ressaiguié T and Chevalier J-M 2012 Gel versus aerogel to collect high velocity ejectas from laser shock-loaded metallic targets for postrecovery analyses *AIP Conf. Proc.* **1426** 120–3
- [32] Maddox B R, Park H-S, Lu C-H, Remington B A, Prisbrey S, Kad B, Luo R and Meyers M A 2013 Isentropic/shock compression and recovery methodology for materials using high-amplitude laser pulses *Mater. Sci. Eng. A* **578** 354–61
- [33] Schuster A K 2021 Recovery of nanodiamonds from dynamically shock-compressed graphite and hydrocarbon samples *PhD Thesis* Technical University of Dresden, Helmholtz-Zentrum Dresden-Rossendorf
- [34] Nagler B *et al* 2015 The matter in extreme conditions instrument at the linac coherent light source *J. Synchrotron Radiat.* **22** 520–5
- [35] Glenzer S H *et al* 2016 Matter under extreme conditions experiments at the linac coherent light source *J. Phys. B: At. Mol. Opt. Phys.* **49** 092001
- [36] Weitkamp T, Tafforeau P, Boller E, Cloetens P, Valade J-P, Bernard P, Peyrin Fçoise, Ludwig W, Helfen L and Baruchel Je 2010 Status and evolution of the ESRF beamline ID19 *AIP Conf. Proc.* **1221** 33–38
- [37] Olbinado M P *et al* 2018 Ultra high-speed x-ray imaging of laser-driven shock compression using synchrotron light *J. Phys. D: Appl. Phys.* **51** 055601
- [38] Bagnoud V *et al* 2010 Commissioning and early experiments of the PHELIX facility *Appl. Phys. B* **100** 137–50
- [39] Barker L M and Hollenbach R E 1972 Laser interferometer for measuring high velocities of any reflecting surface *J. Appl. Phys.* **43** 4669–75
- [40] MacFarlane J J, Golovkin I E and Woodruff P R 2006 HELIOS-CR-A 1-D radiation-magnetohydrodynamics code with inline atomic kinetics modeling *J. Quant. Spectrosc. Radiat. Transfer* **99** 381–97
- [41] Rouseas M, Goldstein A P, Mickelson W, Worsley M A, Woo L and Zettl A 2013 Synthesis of highly crystalline sp<sup>2</sup>-bonded boron nitride aerogels *ACS Nano* **7** 8540–6
- [42] Pham T, Goldstein A P, Lewicki J P, Kucheyev S O, Wang C, Russell T P, Worsley M A, Woo L, Mickelson W and Zettl A 2015 Nanoscale structure and superhydrophobicity of sp<sup>2</sup>-bonded boron nitride aerogels *Nanoscale* **7** 10449–58
- [43] Zettl A K, Rouseas M, Goldstein A P, Mickelson W, Worsley M A and Woo L 2017 Crystalline boron nitride aerogels *US Patent* 9611146
- [44] Benad A, Jürries F, Vetter B, Klemmed B, Hübner Re, Leyens C and Eychmüller A 2017 Mechanical properties of metal oxide aerogels *Chem. Mater.* **30** 145–52
- [45] Jones S M 2010 Non-silica aerogels as hypervelocity particle capture materials *Meteorit. Planet. Sci.* **45** 91–98
- [46] Arnault J-C 2017 *Nanodiamonds: Advanced Material Analysis, Properties and Applications* (Cambridge: The Royal Society of Chemistry)
- [47] Plimpton S 1995 Fast parallel algorithms for short-range molecular dynamics (LAMMPS) *J. Comput. Phys.* **117** 1–19
- [48] O'Connor T C, Andzelm J and Robbins M O 2015 AIREBO-M: a reactive model for hydrocarbons at extreme pressures *J. Chem. Phys.* **142** 024903
- [49] Mishin Y, Farkas D, Mehl M J and Papaconstantopoulos D A 1999 Interatomic potentials for monoatomic metals from experimental data and *ab initio* calculations *Phys. Rev. B* **59** 3393
- [50] Eggert J H, Hicks D G, Celliers P M, Bradley D K, McWilliams R S, Jeanloz R, Miller J E, Boehler T R and Collins G W 2010 Melting temperature of diamond at ultrahigh pressure *Nat. Phys.* **6** 40–43
- [51] Kinslow R 1970 *High Velocity Impact Phenomena* (New York: Academic) p 547
- [52] Watson E and Steinhauser M O 2017 Discrete particle method for simulating hypervelocity impact phenomena *Materials* **10** 379
- [53] Viecelli J A, Bastea S, Glosli J N and Ree F H 2001 Phase transformations of nanometer size carbon particles in shocked hydrocarbons and explosives *J. Chem. Phys.* **115** 2730–6
- [54] Barnard A S 2006 *Stability of nanodiamond Ultrananocrystalline Diamond* ed O A Shenderova and D M Gruen (Norwich, NY: William Andrew Publishing) ch 4, pp 117–54

- [55] Shenderova O A, Zhirnov V V and Brenner D W 2002 Carbon nanostructures *Crit. Rev. Solid State Mater. Sci.* **27** 227–356
- [56] Danilenko V V 2005 Phase diagram of nanocarbon *Combust. Explos. Shock Waves* **41** 460–6
- [57] Melanie R 2022 Coherent x-ray diffraction of laser-driven matter *PhD Thesis* TU Dresden, Helmholtz-Zentrum Dresden Rossendorf
- [58] Xie H, Yin F, Tao Y, Wang J-T and Liang C 2014 Mechanism for direct graphite-to-diamond phase transition *Sci. Rep.* **4** 1–5
- [59] Celliers P M *et al* 2018 Insulator-metal transition in dense fluid deuterium *Science* **361** 677–82
- [60] Helled R, Mazzola G and Redmer R 2020 Understanding dense hydrogen at planetary conditions *Nat. Rev. Phys.* **2** 562–74
- [61] Domínguez G, Westphal A J, Jones S M and Phillips M L F 2004 Energy loss and impact cratering in aerogels: theory and experiment *Icarus* **172** 613–24
- [62] Jay Melosh H 1989 *Impact Cratering: A Geologic Process (Oxford Monographs on Geology and Geophysics vol 11)* (New York: Oxford University Press) p 253 Research supported by NASA
- [63] Holmes N C, Radousky H B, Moss M J, Nellis W J and Henning S 1984 Silica at ultrahigh temperature and expanded volume *Appl. Phys. Lett.* **45** 626–8
- [64] Anderson W W 1998 Physics of interplanetary dust collection with aerogel *NASA STI/Recon Technical Report N* vol 98 (Georgia southwestern coll. Americus, GA) p 97922 (available at: <https://ntrs.nasa.gov/citations/19980107921>)
- [65] Coulson S G 2009 Hydrodynamic modelling of cometary particles captured in aerogel and the Earth's atmosphere *Meteorit. Planet. Sci.* **44** 1421–30
- [66] Coulson S G 2009 On the deceleration of cometary fragments in aerogel *Int. J. Astrobiol.* **8** 9–17
- [67] Jones S M, Anderson M S, Domínguez G and Tsapin A 2013 Thermal calibrations of hypervelocity capture in aerogel using magnetic iron oxide particles *Icarus* **226** 1–9
- [68] Anderson W W and Ahrens T J 1994 Physics of interplanetary dust capture via impact into organic polymer foams *J. Geophys. Res. Planets* **99** 2063–71
- [69] Kadono T 1999 Hypervelocity impact into low density material and cometary outburst *Planet. Space Sci.* **47** 305–18
- [70] Domínguez G 2009 Time evolution and temperatures of hypervelocity impact-generated tracks in aerogel *Meteorit. Planet. Sci.* **44** 1431–43
- [71] Trigo-Rodríguez J M, Domínguez G, Burchell M J, Hörz F and Llorca J 2008 Bulbous tracks arising from hypervelocity capture in aerogel *Meteorit. Planet. Sci.* **43** 75–86
- [72] Anderson W and Ahrens T 2012 Physics of intact capture of cometary Coma dust samples *AIP Conf. Proc.* **1426** 875–8
- [73] Ruhnnow F, Zwicker D and Diez S 2011 Tracking single particles and elongated filaments with nanometer precision *Biophys. J.* **100** 2820–8
- [74] Daly R T and Schultz P H 2018 Projectile preservation during oblique hypervelocity impacts *Meteorit. Planet. Sci.* **53** 1364–90
- [75] Saalfeld S 2010 Enhance local contrast plugin (CLAHE) (available at: [https://imagej.net/Enhance\\_Local\\_Contrast\\_\(CLAHE\)](https://imagej.net/Enhance_Local_Contrast_(CLAHE)))
- [76] Ferrari A C and Robertson J 2004 Raman spectroscopy of amorphous, nanostructured, diamond-like carbon and nanodiamond *Phil. Trans. R. Soc. A* **362** 2477–512
- [77] Mochalin V, Osswald S and Gogotsi Y 2008 Contribution of functional groups to the Raman spectrum of nanodiamond powders *Chem. Mater.* **21** 273–9
- [78] Knight D S and White W B 1989 Characterization of diamond films by Raman spectroscopy *J. Mater. Res.* **4** 385–93
- [79] Osswald S, Yushin G, Mochalin V, Kucheyev S O and Gogotsi Y 2006 Control of sp<sup>2</sup>/sp<sup>3</sup> carbon ratio and surface chemistry of nanodiamond powders by selective oxidation in air *J. Am. Chem. Soc.* **128** 11635–42
- [80] Osswald S 2014 *Nanodiamond purification Nanodiamond* (Cambridge: The Royal Society of Chemistry) ch 4, pp 89–111
- [81] Osswald S, Havel Mel, Mochalin V, Yushin G and Gogotsi Y 2008 Increase of nanodiamond crystal size by selective oxidation *Diam. Relat. Mater.* **17** 1122–6
- [82] Popov M, Churkin V, Kirichenko A, Denisov V, Ovsyannikov D, Kulnitskiy B, Perezhogin I, Aksenenkov V and Blank V 2017 Raman spectra and bulk modulus of nanodiamond in a size interval of 2–5 nm *Nanoscale Res. Lett.* **12** 561
- [83] Adar F 2010 Depth resolution of the Raman microscope: optical limitations and sample characteristics (available at: [www.spectroscopyonline.com/depth-resolution-raman-microscope-optical-limitations-and-sample-characteristics](http://www.spectroscopyonline.com/depth-resolution-raman-microscope-optical-limitations-and-sample-characteristics))
- [84] Korepanov V I, Hamaguchi H, Ōsawa E, Ermolenkov V, Lednev I K, Etzold B J M, Levinson O, Zousman B, Epperla C P and Chang H-C 2017 Carbon structure in nanodiamonds elucidated from Raman spectroscopy *Carbon* **121** 322–9
- [85] Mermoux M, Chang S, Girard H A and Arnault J-C 2018 Raman spectroscopy study of detonation nanodiamond *Diam. Relat. Mater.* **87** 248–60
- [86] LécZ Z, Budai J, Andreev A and Ter-Avetisyan S 2020 Thickness of natural contaminant layers on metal surfaces and its effects on laser-driven ion acceleration *Phys. Plasmas* **27** 013105
- [87] Yasko R N and Whitmoyer R D 1971 Auger electron energies (0–2000 eV) for elements of atomic number 5–103 *J. Vac. Sci. Technol.* **8** 733–7
- [88] Childs K D, Carlson B A, LaVanier L A, Moulder J F, Paul D F, Stickle W F and Watson D G 1995 *Handbook of Auger Electron Spectroscopy. A Book of Reference Data for Identification and Interpretation in Auger Electron Spectroscopy* 3rd edn (Minnesota: Physical Electronics, Inc.) (available at: [https://openlibrary.org/books/OL22399332M/Handbook\\_of\\_auger\\_electron\\_spectroscopy](https://openlibrary.org/books/OL22399332M/Handbook_of_auger_electron_spectroscopy))
- [89] Donnelly E and Mothe F 2013 Polar transformer (available at: <https://imagej.nih.gov/ij/plugins/polar-transformer.html>)
- [90] Bunch T E, Becker L, Bada J, Macklin J, Radicatidibrozolo F, Fleming R H and Erlichman J 1993 Hypervelocity impact survivability experiments for carbonaceous impactors (N93-29364) (NASA Ames Research Center)
- [91] Bunch T E, Paque J M, Becker L and Vedder J F 1993 Hypervelocity impact survivability experiments for carbonaceous impactors: part II *NASA Conf. Publication* (NASA) p 385
- [92] Holleman A F and Wiberg E 1985 *Lehrbuch der Anorganischen Chemie* (Berlin: De Gruyter)
- [93] Zousman B and Levinson O 2014 Pure nanodiamonds produced by laser-assisted technique *Nanodiamond* (Cambridge: Royal Society of Chemistry) pp 112–27
- [94] Perevedentseva E, Peer D, Uvarov V, Zousman B and Levinson O 2015 Nanodiamonds of laser synthesis for biomedical applications *J. Nanosci. Nanotechnol.* **15** 1045–52
- [95] Mochalin V N, Shenderova O, Ho D and Gogotsi Y 2012 The properties and applications of nanodiamonds *Nat. Nanotechnol.* **7** 11
- [96] Barthel K U 2012 Fiji plugin: volume viewer (available at: <https://imagej.nih.gov/ij/plugins/volume-viewer.html>)
- [97] Bruker 2011 CTvox quick start guide for software version 2.2 (available at: [https://umanitoba.ca/faculties/health\\_sciences/medicine/units/cacs/sam/media/CTvox\\_QuickStartGuide.pdf](https://umanitoba.ca/faculties/health_sciences/medicine/units/cacs/sam/media/CTvox_QuickStartGuide.pdf))